



A framework to evaluate and elucidate the driving mechanisms of coastal sea surface pCO₂ seasonality using an ocean general circulation model (MOM6-COBALT)

5 **Alizée Roobaert**¹, Laure Resplandy², Goulven G. Laruelle¹, Enhui Liao² and Pierre Regnier¹

¹Department of Geosciences, Environment & Society-BGEOSYS, Université Libre de Bruxelles, Brussels, CP160/02, Belgium

²Department of Geosciences, Princeton University, Princeton, NJ, USA

10

Correspondence to: Alizée Roobaert (Alizee.Roobaert@ulb.be)

Abstract

The temporal variability of the sea surface partial pressure of CO₂ (pCO₂) and the underlying processes driving this variability are poorly understood in the coastal ocean. In this study, we tailor an existing method that quantifies the effects of thermal changes, biological activity, ocean circulation and fresh water fluxes to examine seasonal pCO₂ changes in highly-variable coastal environments. We first use the Modular Ocean Model version 6 (MOM6) and biogeochemical module Carbon Ocean Biogeochemistry And Lower Trophics version 2 (COBALTv2) at a half degree resolution to simulate the coastal CO₂ dynamics and evaluate it against pCO₂ from the Surface Ocean CO₂ Atlas database (SOCAT) and from the continuous coastal pCO₂ product generated from SOCAT by a two-step neuronal network interpolation method (coastal-SOM-FFN, Laruelle et al., 2017). The MOM6-COBALT model not only reproduces the observed spatio-temporal variability in pCO₂ but also in sea surface temperature, salinity, nutrients, in most coastal environments except in a few specific regions such as marginal seas. Based on this evaluation, we identify coastal regions of ‘high’ and ‘medium’ model skill where the drivers of coastal pCO₂ seasonal changes can be examined with reasonable confidence. Second, we apply our decomposition method in three contrasted coastal regions: an Eastern (East coast of the U.S) and a Western (the Californian Current) boundary current and a polar coastal region (the Norwegian Basin). Results show that differences in pCO₂ seasonality in the three regions are controlled by the balance between ocean circulation, biological and thermal changes. Circulation controls the pCO₂ seasonality in the Californian Current, biological activity controls pCO₂ in the Norwegian Basin, while the interplay between biology, thermal and circulation changes is key in the East coast of the U.S. The refined approach presented here allows the attribution of pCO₂ changes with small residual biases in the coastal ocean, allowing future work on the mechanisms controlling coastal air-sea CO₂ exchanges and how they are likely to be affected by future changes in sea surface temperature, hydrodynamics and biological dynamics.

15
20
25
30



1 Introduction

The ocean plays an important role in offsetting human-induced carbon dioxide (CO₂) emissions associated with cement production and fossil fuel combustion (Friedlingstein et al., 2019). Globally, the ocean is a net sink that absorbs roughly one
35 quarter of the anthropogenic CO₂ emitted into the atmosphere (-2.5 ± 0.6 Petagram of carbon per year (Pg C yr⁻¹) for the 2009-2018 decade, Friedlingstein et al., 2019). The spatio-temporal variability of this oceanic CO₂ uptake is relatively well constrained in the open ocean thanks to several methods including sea surface CO₂ data-derived interpolations (e.g., Landschützer et al., 2014; Rödenbeck et al., 2014, 2015; Takahashi et al., 2002), models and atmospheric inversions (e.g., Gruber et al., 2009, 2019; Keeling and Manning, 2014; Manning and Keeling, 2006), but it is less constrained and understood
40 in the coastal ocean. Nonetheless, in recent decades, significant progress has been made with regard to the quantification and analysis of the spatial distribution of the coastal air-sea CO₂ exchange (FCO₂) globally and regionally (e.g., Borges et al., 2005; Cai, 2011; Chen et al., 2013; Laruelle et al., 2010, 2014, Roobaert et al., 2019). The FCO₂ seasonal cycle was also recently analyzed in coastal regions worldwide by Roobaert et al. (2019). This study identified that at the annual timescale, the global coastal ocean acts as an atmospheric CO₂ sink (-0.2 ± 0.02 Pg C yr⁻¹) with a more intense CO₂ uptake occurring in summer
45 because of the disproportionate influence of high latitude coastal seas in the Northern Hemisphere. A more in-depth analysis also revealed that the majority of the coastal seasonal FCO₂ variations stems from the air-sea gradient in partial pressure of CO₂ (pCO₂), although changes in wind speed and sea-ice cover can be significant regionally.

Several processes influence the seasonal variations of surface ocean pCO₂ and thus, the seasonality in FCO₂. These processes
50 include changes in sea surface temperature (SST) tied to air-sea heat fluxes and ocean circulation, changes in sea surface salinity (SSS) associated with evaporation, fresh water fluxes (from land, ice-melt, precipitation and evaporation) and ocean circulation, as well as variations in sea surface alkalinity (ALK) and dissolved inorganic carbon (DIC) tied to biological activity, fresh water fluxes and ocean circulation (Sarmiento and Gruber, 2006). In the open ocean, the respective influence of these processes on the pCO₂ variability has been interpreted using changes in SST, SSS, ALK and DIC observed in-situ (e.g.,
55 Landschützer et al., 2018; Takahashi et al., 1993) or based on global/regional ocean biogeochemical models relying on a mechanistic, quantitative description of the physical, chemical and biological processes controlling the ocean carbon cycle (e.g., Doney et al., 2009). These investigations reveal that changes in SST (i.e. the thermal effect) is the main driver of the seasonal pCO₂ in tropical oceanic regions, while non-thermal components (change associated with DIC, ALK and SSS) dominate at mid- and high-latitude (poleward of 40° N and 40° S, e.g., Landschützer et al., 2018; Takahashi et al., 2002).

60 In the coastal ocean, the processes controlling the pCO₂ seasonal dynamics were mostly investigated regionally (e.g., Arruda et al., 2015; Frankignoulle & Borges, 2001; Laruelle et al., 2014; Nakaoka et al., 2006; Shadwick et al., 2010, 2011; Signorini et al., 2013; Turi et al., 2014; Yasunaka et al., 2016) and only a few observation-based studies attempted to analyze the coastal pCO₂ seasonal variability into processes at the global scale (Cao et al., 2020; Chen and Hu, 2019; Laruelle et al., 2017).



65 Regional studies using either observations or model results have covered, e.g., the shelves of the entire Atlantic basin (Laruelle
et al., 2014), the West (California Current, Turi et al., 2014) and East (e.g., Shadwick et al., 2010, 2011; Signorini et al., 2013)
coasts of the United States, as well as the South and Southeast Brazilian shelves, Uruguayan and Patagonia shelves and shelves
along the southwestern Atlantic ocean (Arruda et al., 2015). In the California Current, the strong upwelling of carbon-rich
waters was identified as the main control of the pCO₂ seasonality (Turi et al. 2014). On the Patagonia shelf, the thermal effect
70 and biological pumps were found to be the main drivers of the seasonal pCO₂ variability with only a small contribution from
the ocean circulation (Arruda et al., 2015), while along the East coast of the U.S, seasonal thermal changes play the major role
(Shadwick et al., 2010, 2011; Laruelle et al., 2015; Signorini et al., 2013). These studies are, however, confined to specific
regions and a global picture of the mechanisms driving the coastal pCO₂ dynamics is still missing. In addition, the attribution
analysis into specific physical and biological processes is incomplete. Indeed, the attribution relies on a linear decomposition
75 linking variations in sea surface ocean pCO₂ to seasonal changes in DIC, ALK, SST and SSS (e.g., Signorini et al., 2013,
Doney et al., 2009; Lovenduski et al., 2007; Takahashi et al., 1993; Turi et al., 2014), or on a series of sequential simulations
isolating biological and physical terms therefore ignoring how covariations between the different terms dampen or reinforce
each other (e.g., Arruda et al., 2015; Turi et al., 2014).

80 In this study, we develop a new framework to elucidate the seasonal pCO₂ dynamics of the global coastal ocean. This
framework relies on the global Modular Ocean Model version 6 (MOM6, Adcroft et al., 2019) from the NOAA Geophysical
Fluid Dynamics Laboratory coupled to the biogeochemical module Carbon Ocean Biogeochemistry And Lower Trophics
version 2 (COBALTv2, Stock et al., 2014, 2020). MOM6-COBALT model outputs provide the relevant variables and
processes that are required to perform an explicit decomposition of the inorganic carbon dynamics (Liao et al., 2020) in the
85 entire coastal domain. These outputs are then analyzed using a novel approach to attribute seasonal variations in surface ocean
pCO₂ to changes in biological activity, ocean circulation, SST, air-sea CO₂ fluxes and fresh water fluxes (Liao et al., 2020),
and which is here enhanced for the coastal ocean. The decomposition method constitutes a significant improvement upon
previous studies. First, it accounts for co-variations in biological and physical processes and how their evolution jointly
modulates the pCO₂ signal. Second, it improves on the traditional linear approaches developed for the open ocean (Sarmiento
90 and Gruber, 2006; Takahashi et al., 1993) and used since then (e.g. Lovenduski et al., 2007), because, as shown later in this
study, the linear decomposition introducing significant biases in coastal waters due to the larger range in DIC, ALK, pH and
salinity values encountered in the variable coastal environment (Egleston et al., 2010).

In light of these knowledge gaps, the objective of this paper are twofold:

- 95 - First, we evaluate the performance of the MOM6-COBALT model in its ability to reproduce the observed spatio-
temporal fields of SSS, SST, sea surface nutrients and pCO₂ in the global coastal domain. In particular, we identify
the coastal regions where the model best reproduces the observed ocean pCO₂ variability and can thus be considered
most suitable for a detailed analysis of the drivers of the pCO₂ seasonal changes.



100 - Second, to illustrate the capabilities of our upgraded decomposition framework, we examine the drivers of the pCO₂ seasonality in three contrasted coastal regions: The East coast of the U.S, the West coast of North America and the Norwegian Basin.

2 Methodology

2.1 Ocean biogeochemical model description

105 In this study, we used the ocean model MOM6 and the Sea Ice Simulator version 2 (fourth generation of ocean-ice models called OM4) detailed in Adcroft et al. (2019). The version of OM4 adopted here is OM4p5 which has a nominal horizontal resolution of 0.5° (i.e. with a finer latitudinal resolution of 0.26° in the tropical region). On the vertical, it includes 75 hybrid coordinates with a z* coordinate near the surface (geopotential coordinate allowing free surface undulations) and a modified potential density coordinate below. The vertical spacing increases from 2 m in the upper 20 m (i.e first 10 layers) to larger isopycnal layers below. Layers in z* broadly deepens towards high latitudes (see Adcroft et al., 2019 for details on the grid).

110 This ocean-ice model is coupled to the biogeochemical module COBALT version 2 (COBALTv2), which includes 33 state variables to resolve global-scale cycles of carbon, nitrogen, phosphate, silicate, iron, calcium carbonate, oxygen and lithogenic materials (Stock et al., 2020). Details about the planktonic food web dynamics in COBALT, and global assessments of large-scale carbon fluxes through the food web such as net primary production can be found in Stock et al. (2014, 2020). The ocean model is forced by the 55-km horizontal resolution Japanese atmospheric reanalysis (JRA55-do) version 1.3 at a 3-hour

115 frequency between 1959 and 2018 (Tsuji no et al., 2018), and the atmospheric pCO₂ data from the Earth System Research Laboratory (Joos and Spahni, 2008). SST, SSS, sea surface nutrients (nitrate, phosphate, silicate) and oxygen were initialized from the World Ocean Atlas version 2013 (Garcia et al., 2013a, 2013b; Locarnini et al., 2013; Zweng et al., 2013). Initial DIC and ALK conditions are taken from GLODAPv2 (Olsen et al., 2016). The initial DIC is corrected for the accumulation of anthropogenic carbon to match the level expected in the first year of simulation (1959) using the data-based estimate of ocean

120 anthropogenic carbon content of Khatiwala et al. (2013). At the end of a 81-year spin-up repeating year 1959, the model has reached a near-equilibrium between atmospheric pCO₂ and surface ocean pCO₂, with a drift in global air-sea CO₂ flux < 0.004 Pg C yr⁻¹ over the last 10 years of spin-up. Further details on the configuration, spin-up and simulation can be found in Liao et al. (2020).

2.2 Observational products and model evaluation

125 We first evaluate the ability of MOM6-COBALT to reproduce the observed spatial distribution of environmental variables in the coastal domain, namely the SST, SSS and sea surface nutrients (nitrate, phosphate and silicate). The observational SST and SSS fields are from the daily NOAA OI SST V2 (Reynolds et al., 2007) and the daily Hadley center EN4 SSS (Good et al., 2013), respectively. The observed nutrient fields in the sea surface are extracted from the World Ocean Atlas version 2018 (Garcia et al., 2019). We also compare the simulated coastal pCO₂ directly to “raw”, un-interpolated observations extracted



130 from the Surface Ocean CO₂ Atlas database (SOCAT), using monthly observations from SOCAT version 6 gridded at the
spatial resolution of 0.25 degree (SOCATv6, Bakker et al., 2016). For the evaluation period used in this study (1998 - 2015),
this database contains 9.8 million pCO₂ observations within the coastal domain. All data from SOCATv6 are converted from
fugacity of CO₂ in water to pCO₂ using the formulation of Takahashi et al. (2012). We finally compare the pCO₂ simulated by
the MOM6-COBALT model to the 0.25° continuous monthly pCO₂ fields generated from the SOCAT observations by the
135 two-step neuronal network (SOM-FFN) in coastal regions (Laruelle et al., 2017). The SOM-FFN data product of Laruelle et
al. (2017) is thus not “raw” and implies a significant amount of statistical modelling. It is also derived from an earlier version
of SOCAT (SOCATv4, Laruelle et al., 2017) than the “raw” one. In what follows, the pCO₂ products generated by the model,
the statistical interpolation of observations, and the un-interpolated observations will be referred to as MOM6-COBALT,
coastal-SOM-FFN and Socatv6, respectively. All observational and simulated fields are converted from their original spatio-
140 temporal resolution to monthly 0.25° gridded climatologies for the 1998 - 2015 period to match the one used by the coastal-
SOM-FFN. Cells that are covered by more than 95 % of sea-ice are removed from the comparison since we assume no transfer
of our master variable (pCO₂) through sea ice. In our analysis, we apply the broad definition of the coastal zone by Laruelle et
al. (2017), using a global mask that excludes estuaries and inland water bodies while its outer limit is set 300 km away from
the shoreline. This definition leads to a total surface area of 77 million km² which is split into 45 coastal regions using the
145 MARGins and CATchment Segmentation (MARCATS, Laruelle et al., 2013). These 45 regions are grouped into 7 broad
classes with similar hydrological and climatic settings (Liu et al., 2010): (1) Eastern and (2) Western Boundary Currents (EBC
and WBC respectively), (3) tropical margins, (4) subpolar and (5) polar margins, (6) marginal seas and (7) Indian margins.

The model evaluation of all gridded environmental variables including pCO₂ is performed for the annual mean and the seasonal
150 cycle both globally and within each of the 45 MARCATS regions. For the seasonal analysis, for each variable, a climatological
monthly anomaly is calculated as the difference between the variable *x* for a given month and its climatological annual mean.
The evaluation of the seasonal amplitude is then performed using the bias between observed and simulated root mean square
(RMS) of their monthly anomalies. A positive bias represents a larger simulated seasonal amplitude than derived from the
observations. The temporal shift between observed and simulated seasonal cycles is also assessed from the Pearson correlation
155 coefficient (no units) of the regression between monthly times series simulated by MOM6-COBALT and those extracted from
the observations. These comparisons not only serve to assess the overall model’s performance in reproducing observations but
also help identifying potential discrepancies between observed and simulated environmental fields (e.g., SST, SSS) that are
used by the two-step neuronal network coastal-SOM-FFN to generate the continuous pCO₂ climatology.

160 Finally, from this global and regional spatio-temporal evaluation, we label the model skill (‘high’, ‘medium’ and ‘low’) for
each MARCATS and identify regions for which our results are the most robust for further in-depth analysis of the processes
driving the coastal pCO₂ dynamics. The model skill labelling is based on 3 criteria: First, we assess whether the simulated
annual mean pCO₂ is within 20 μatm of the one extracted from the coastal-SOM-FFN. This threshold of 20 μatm roughly



corresponds to the globally averaged pCO₂ gradient between the atmosphere and the coastal sea surface (Laruelle et al., 2018).
165 The second and third criteria evaluate the magnitude and phasing of the simulated pCO₂ seasonal cycle against the coastal-SOM-FFN, using an absolute bias in the seasonal magnitude < 20 μatm and a Pearson coefficient > 0.5 as threshold. Model skill is considered ‘high’ when the 3 criteria are fulfilled, ‘medium’ when criteria 2 and 3 are satisfied and ‘low’ when only one or zero criteria is met on the seasonality.

2.3 Processes controlling seasonal pCO₂ variability: a method tailored for coastal regions

170 pCO₂ in surface sea water can be computed from DIC and ALK following Eq. (1) (Sarmiento and Gruber, 2006; Wolf-Gladrow et al., 2007):

$$pCO_2 = \frac{K_2'}{K_0'K_1'} \frac{(2DIC - ALK)^2}{ALK - DIC} \quad (1)$$

175 where K₀' is the aqueous-phase solubility constant of CO₂ in water and K₁' and K₂' represent the apparent equilibrium dissociation constants of the carbonate system. Several physical and biogeochemical processes can thus affect pCO₂ via changes in DIC, ALK and/or via the $\frac{K_2'}{K_0'K_1'}$ term which depends on SST and SSS. To quantify the processes controlling the pCO₂ variability at the seasonal timescale of interest to this study, we adopt the method of Liao et al. (2020). The method starts from the traditional approach that links variations in sea surface ocean pCO₂ to changes in DIC, ALK, SST and SSS using the
180 following linear decomposition (Doney et al., 2009; Lovenduski et al., 2007; Takahashi et al., 1993; Turi et al., 2014):

$$\Delta pCO_2 \approx \frac{\partial pCO_2}{\partial DIC} \Delta DIC + \frac{\partial pCO_2}{\partial ALK} \Delta ALK + \frac{\partial pCO_2}{\partial SST} \Delta SST + \frac{\partial pCO_2}{\partial SSS} \Delta SSS \quad (2)$$

Where the “Δx” terms represent the seasonal anomaly of x (i.e. the departure from the annual mean) and $\frac{\partial pCO_2}{\partial DIC}$, $\frac{\partial pCO_2}{\partial ALK}$, $\frac{\partial pCO_2}{\partial SST}$
185 and $\frac{\partial pCO_2}{\partial SSS}$ are coefficients that describe the sensitivity of pCO₂ to changes in DIC, ALK, SST and SSS. The coefficients for DIC, SST and SSS are always positive as pCO₂ increases with increases in DIC, SST or SSS, while the coefficient for ALK is always negative as pCO₂ systematically decreases with increasing ALK. These coefficients are generally estimated using the approach of Sarmiento and Gruber (2006) (see Eq. S1-S4 in Appendix), which has been widely used in the open ocean (Liao et al., 2020; Sarmiento and Gruber, 2006; Takahashi et al., 1993). In this study, we refine the estimation of the coefficients so
190 they can be used for the wide range of DIC/ALK ratios that can be encountered in the coastal waters. This includes conditions when the DIC/ALK ratio is close to 1, such as in regions with significant freshwater discharge like those found near estuarine mouths or on polar shelves subject to sea-ice melting, when pH is around 7.5 (Egleston et al., 2010). In these case, the traditional approximation method breaks down (see Eq. (S1-S2) and Figure S1 in the Appendix). To circumvent this important limitation, we computed the coefficients of the pCO₂ dependency using a regression approach based on the CO2SYS program



195 (Lewis and Wallace, 1998). At each point in space, $p\text{CO}_2$ was computed using the 1998 - 2015 average of DIC, ALK, SSS and
 SST with CO2SYS (method 14 in CO2SYS Matlab program, Millero, 2010). The $\frac{\partial p\text{CO}_2}{\partial \text{DIC}}$ coefficient was then computed as the
 slope of the linear regression between $p\text{CO}_2$ and DIC obtained by allowing DIC to vary around the local mean DIC value while
 keeping other tracers (ALK, SST, SSS) constant. The DIC range used to compute the slope was set to the ± 2 standard deviation
 of the 1998-2015 monthly values at that location with an upper bound at $\pm 60 \mu\text{mol kg}^{-1}$ (see Appendix for further details).
 200 The same approach was repeated to compute the coefficients for the $p\text{CO}_2$ dependence on ALK, SST and SSS, respectively.
 Our methodology leads to coefficients that are constant in time but space dependent. In Fig. S1, we compare the coastal $p\text{CO}_2$
 reconstructed from the traditional decomposition (using the empirical coefficients reported by Sarmiento and Gruber, 2006)
 with those computed here. For the global coastal ocean, we find a large bias (global mean rmse of fitting $p\text{CO}_2$ anomaly in Eq.
 (2) = $14.6 \mu\text{atm}$), which is especially pronounced at high latitudes. In contrast, the decomposition method based on our
 205 methodology reduce drastically the biases (global mean rmse = $2.8 \mu\text{atm}$) in coastal regions and allows a more robust
 reconstruction of the $p\text{CO}_2$ variability.

Here we assume that the coefficients are constant in time, and the temporal change in $p\text{CO}_2$ ($\partial_t p\text{CO}_2$ in $\mu\text{atm month}^{-1}$) can
 therefore be expressed as a simple function of the temporal changes in DIC ($\partial_t \text{DIC}$), ALK ($\partial_t \text{ALK}$), SST ($\partial_t \text{SST}$) and SSS
 210 ($\partial_t \text{SSS}$):

$$\partial_t p\text{CO}_2 \approx \frac{\partial p\text{CO}_2}{\partial \text{DIC}} \partial_t \text{DIC} + \frac{\partial p\text{CO}_2}{\partial \text{ALK}} \partial_t \text{ALK} + \frac{\partial p\text{CO}_2}{\partial \text{SST}} \partial_t \text{SST} + \frac{\partial p\text{CO}_2}{\partial \text{SSS}} \partial_t \text{SSS} \quad (3)$$

Temporal changes in DIC, ALK, SST, and SSS ($\partial_t \text{DIC}$, $\partial_t \text{ALK}$, $\partial_t \text{SST}$ and $\partial_t \text{SSS}$) are controlled by surface heat flux, ocean
 215 transport, freshwater fluxes, biological processes, and the air-sea CO_2 flux. Using the model results, we further expand the
 decomposition to quantify the contribution of these physical and biological processes (see details of derivation in Liao et al,
 2020) :

$$\begin{aligned} & \frac{\partial_t p\text{CO}_2}{p\text{CO}_2 \text{ change}} \approx \\ 220 & \underbrace{\left(\frac{\partial p\text{CO}_2}{\partial \text{DIC}} \partial_t \text{DIC}_h + \frac{\partial p\text{CO}_2}{\partial \text{ALK}} \partial_t \text{ALK}_h + \frac{\partial p\text{CO}_2}{\partial \text{SSS}} \partial_t \text{SSS}_h + \frac{\partial p\text{CO}_2}{\partial \text{DIC}} \partial_t \text{DIC}_v + \frac{\partial p\text{CO}_2}{\partial \text{ALK}} \partial_t \text{ALK}_v + \frac{\partial p\text{CO}_2}{\partial \text{SSS}} \partial_t \text{SSS}_v \right)}_{\text{circ}} \\ & + \underbrace{\left(\frac{\partial p\text{CO}_2}{\partial \text{DIC}} \partial_t \text{DIC}_{fw} + \frac{\partial p\text{CO}_2}{\partial \text{ALK}} \partial_t \text{ALK}_{fw} + \frac{\partial p\text{CO}_2}{\partial \text{SSS}} \partial_t \text{SSS}_{fw} \right)}_{fw} \\ & + \underbrace{\left(\frac{\partial p\text{CO}_2}{\partial \text{DIC}} \partial_t \text{DIC}_{bio} + \frac{\partial p\text{CO}_2}{\partial \text{ALK}} \partial_t \text{ALK}_{bio} \right)}_{bio} \end{aligned}$$



$$\begin{aligned} & + \underbrace{\left(\frac{\partial pCO_2}{\partial T} (\partial_t SST_h + \partial_t SST_v + \partial_t SST_q)\right)}_{thermal} \\ & + \underbrace{\left(\frac{\partial pCO_2}{\partial DIC} \partial_t DIC_{CO_2 flux}\right)}_{CO_2 flux} \end{aligned} \quad (4)$$

225

where the temporal changes in pCO₂ (time tendency called *pCO₂ change*) is on the left-hand side (LHS), and the five terms that control this change in pCO₂ are on the right-hand side (RHS) of the equation. Subscripts *h* and *v* denote the contribution from horizontal (advection and diffusivity in the meridional and zonal directions) and vertical (vertical advection and diffusivity) transports on SST, SSS, DIC and ALK, *bio* denotes the DIC and ALK changes induced by biological processes (photosynthesis, respiration, and calcium carbonate dissolution/precipitation, denitrification and nitrification), *q* denotes the effect of surface heat flux on SST, *fw* denotes the effect of fresh water fluxes (i.e., precipitation, evaporation, river runoff and sea-ice formation and melting) on SSS, DIC and ALK, and the term *CO₂ flux* denotes the DIC change induced by air-sea CO₂ exchange.

230

235

Here we examine changes in pCO₂ attributed to three oceanic processes that modify the concentration in dissolved species (i.e. DIC, ALK and SSS), namely their transport by oceanic circulation (*circ*, which include horizontal and vertical transport), the effect of dilution/concentration due to freshwater fluxes (*fw*) and the effect of biological activity (*bio*), and isolate the *thermal* influence tied to SST changes induced by both oceanic transport and air-sea exchange of heat. Finally, the air-sea CO₂ exchange (*CO₂ flux*) pushes the surface pCO₂ concentration towards its equilibrium with the atmosphere and systematically acts to offset the pCO₂ changes associated with the sum of the internal oceanic processes (*circ*, *bio*, *fw* and *thermal*). In this study, we apply Eq. (4) using averages between the sea surface and the mixed layer depth (MLD), defined here as the depth where the water density is 0.01 kg m⁻³ denser than the water at the surface (minimum MLD is 5 meters). Positive contributions on the RHS would yield an increase in pCO₂ (positive pCO₂ response on the LHS). Positive values of the *CO₂ flux* correspond to an ocean CO₂ uptake. This method to decompose the pCO₂ seasonality into controlling processes in the coastal domain is illustrated in three coastal regions: The East and West coast of North America and in the Norwegian Basin.

240

245

3 Results and discussion

3.1 Annual mean state and seasonal cycle model evaluation and identification of coastal regions

Figure 1a identifies the coastal regions where the performance of MOM6-COBALT is satisfactory for both the annual mean and the seasonal cycle of pCO₂. The analysis, performed at the MARCATS scale (see Fig. 1b for nomenclature), distinguishes regions of low, medium and high model skill, the latter being areas for which our confidence in the identification of the dominant biophysical drivers of the coastal pCO₂ dynamics is highest. This figure will be analyzed in detail in Section 3.1.3, but before we do so we first perform a data-model evaluation according to the following: We first evaluate the model by

250



comparing simulated fields of SSS, SST, sea surface nutrients to observations globally and regionally (Sect. 3.1.1, Figs. 2 and 3). Second, the ability of the model to capture the coastal pCO₂ annual mean and seasonality is assessed against the “raw”
255 Socatv6 data and the continuous monthly observational-based pCO₂ product (coastal-SOM-FFN, Laruelle et al., 2017), respectively (Sect. 3.1.2, Figs. 3-6).

3.1.1 Model evaluation for coastal waters environmental variables

MOM6-COBALT captures fairly well the main spatial patterns of key environmental parameters (SST, SSS and sea surface nutrients) in the coastal domain (Fig. 2). The global SST field simulated by the model reproduces the strong large-scale tropical
260 to polar SST gradients, with a global median bias of -0.2 °C (Fig. 2a-c), and biases at the scale of MARCATS regions ranging from 0 °C in the North East Atlantic (M17) to 1.3 °C in the East coast of the U.S (M10, Fig. 3a and Table S1). With a global median bias value of 0.2, the model also correctly reproduces the observed SSS patterns which are mainly regulated by evaporation and freshwater inputs from precipitation, riverine runoff and ice melt, with lower SSS values in polar regions and along the coasts in Southeast Asia and higher SSS values along the coasts of evaporation basins such as in the Arabian or the
265 Mediterranean Sea (Fig. 2d-f). The SSS analysis at the MARCATS scale reveals absolute SSS biases generally less than or close to 1 except for five MARCATS where absolute biases exceed 2. These MARCATS are mainly located in marginal seas (the Baltic Sea, M18, the Black Sea, M21 and the Persian Gulf, M29), but also include one polar region (the Canadian Archipelago, M13) and one tropical region (Tropical West Atlantic, M7, Fig. 3b and Table S1). Similar to SSS, largest model-data discrepancies for nutrients are mostly found in marginal seas (Fig. 3c-e and Table S1). For instance, the largest PO₄ and
270 SiO₄ biases are encountered in the Black Sea (M21, absolute biases of 3 and 75 μmol kg⁻¹, respectively). The Peruvian upwelling (M4), the Bay of Bengal (M31) and the N-E Pacific (M1) also present large biases in NO₃ and PO₄, respectively (e.g., NO₃ bias of 8 μmol kg⁻¹ for M4). The global median nutrients biases are however much smaller, reaching 0.3, -0.2 and -0.4 μmol kg⁻¹ for nitrate (NO₃, Fig. 2i), phosphate (PO₄, Fig. 2l) and silicate (SiO₄, Fig. 2o), respectively,

The model-data seasonal evaluation reveals that MOM6-COBALT reproduces the global SST and SSS amplitudes remarkably
275 well (median absolute bias of 0.1 °C and 0.0, respectively, Table S2). Some exceptions can nevertheless be diagnosed such as in the marginal Black Sea (M21) where the bias in SST seasonal amplitude reaches -1.3 °C, and in three MARCATS (The Bay of Bengal (M31), the Tropical West Atlantic (M7), and the Siberian Shelves (M43)) where the SSS seasonal biases are larger than 0.4. The model-data comparison also reveals that the phasing of the SST and SSS seasonal cycles are in very good agreement (Pearson correlation close to 1) for all 45 MARCATS but four, for which significant deviations in SSS are found:
280 two marginal seas (Hudson Bay, M12 and the Red Sea, M28) and along the Californian (M2) and Brazilian Currents (M6). The nutrients analysis shows absolute global median biases in seasonal amplitude of 0.1, 0.0 and 0.7 μmol kg⁻¹ for NO₃, PO₄ and SiO₄, respectively. Seven MARCATS present absolute biases larger than 1.5 μmol kg⁻¹ mainly located in marginal seas (Baltic Sea, M18 and the seas of Japan (M40) and Okhotsk (M41)), but also in polar (Siberian (M43) and Antarctic (M45) shelves) and subpolar (N-E Pacific, M1) regions and in the Bay of Bengal (M31). The model-data comparison sometimes



285 shows significant phases shift in their seasonal signal (Pearson coefficient < 0.5), such as for MARCATS located in Indian and Tropical margins, marginal seas and EBCs.

3.1.2 Model evaluation for coastal $p\text{CO}_2$

The spatial distribution of the annual mean $p\text{CO}_2$ simulated by MOM6-COBALT is in good agreement with the observational $p\text{CO}_2$ values extracted from the “raw” Socatv6 database with generally low $p\text{CO}_2$ values (blue colors) in temperate and high latitudes and high $p\text{CO}_2$ values (yellow and red colors) in tropical and sub-tropical regions (contrast Fig. 4a with Fig. 4b). The model-data $p\text{CO}_2$ evaluation at the regional scale shows that 33 of the 45 MARCATS present absolute biases lower than 20 μatm (Table S1). The regions where the bias exceeds this threshold include two EBC’s (M2 and M4), two marginal seas (M40 and M41), and one Polar (M45), subpolar (M42) and Tropical East Atlantic (M23) shelf. Note that in some MARCATS regions, in particular in marginal seas and Indian seas, there are no Socatv6 observations to perform the comparison (e.g. the Bay of Bengal, M31, see Fig. 4b and Table S1). Hence, we also evaluate the performance of MOM6-COBALT against the continuous coastal-SOM-FFN $p\text{CO}_2$ product which uses a neural network interpolation method to fill data gaps and resolve the spatio-temporal coastal $p\text{CO}_2$ variability globally.

Our results show that MOM6-COBALT reproduces the main spatial features of the annual mean $p\text{CO}_2$ field captured by the coastal-SOM-FFN product, as revealed by the relatively low globally averaged bias of 2.5 μatm (Figs. 4a and 4c). In both the model and the SOM-FFN product, low coastal $p\text{CO}_2$ values are consistently found in temperate and high latitude regions in both hemispheres, while high $p\text{CO}_2$ values are largely limited to (sub)tropical regions. Largest discrepancies (Fig. 4d) are found at high latitudes (poleward of 60° N and 60° S, negative bias), along the Eastern Boundary Peruvian and Namibian upwelling systems (high positive bias) and more locally close to the mouth of some large rivers (e.g., the plume of the Amazon or the Rio de la Plata, high negative bias). We note however that these regions are poorly sampled in the Socatv6 dataset (Fig. 4b) and are thus likely weakly constrained in the coastal-SOM-FFN product (Fig. 4c).

At the regional scale, differences in annual mean $p\text{CO}_2$ between MOM6-COBALT and coastal-SOM-FFN are lower than 20 μatm in 35 MARCATS (Table S1, Fig. 3f), which partly is a reflection of the low annual mean biases observed in the environmental driver variables in these regions (see Sect. 3.1.1). In EBC, WBC, and subpolar coastal regions, the model tends to overestimate the regional mean $p\text{CO}_2$ compared to coastal-SOM-FFN (positive bias), except along the East coast of U.S (M10), in the China and Kuroshio seas (M39) and in the North East Atlantic (M17, Table S1). In polar regions, the model generally underestimates the mean $p\text{CO}_2$ compared to coastal-SOM-FFN, except around the South of Greenland (M15). In Indian, marginal, and tropical coastal regions, no general trend can be identified regarding the sign of the bias, which can be positive or negative.



Quantitatively, the 10 MARCATS with absolute biases $> 20 \mu\text{atm}$ are mainly located in regions for which very limited or no
315 observational data have been compiled in the Socatv6 database (Table S1) and/or for which large discrepancies can already be
identified at the level of the master environmental variables (Sect. 3.1.1). These regions belong mainly to EBCs (3 out of the
6 EBC MARCATS), marginal seas (3 out of the 9 marginal seas MARCATS), the remaining four being either polar (M13 and
M14), subpolar (M42) or Indian margins (M31). The largest biases are found in the Peruvian upwelling Current (M4), the
South West of Africa (M24), the Californian upwelling Current (M2) and the Canadian Archipelago (M13) with biases of 106
320 μatm , 79 μatm , 35 μatm and -53 μatm , respectively.

Our analysis reveals that the seasonal amplitudes simulated by MOM6-COBALT are systematically larger than the ones
estimated by the coastal-SOM-FFN product (Fig. 5a-b, red colors in Fig. 5c and positive biases in Table S2) for all coastal
regions belonging to EBC, WBC, Indian and tropical margins. For the majority of polar and subpolar margins and for some
marginal seas, the model simulates lower seasonal pCO_2 amplitudes (blue colors in Fig. 5c and negative biases in Table S2).
325 Note that the seasonal evaluation is only performed against the coastal-SOM-FFN product because only few 0.25° coastal cells
(approximately 45) in the Socatv6 database contain complete continuous pCO_2 time series. Quantitatively, absolute biases
between the modelled and coastal-SOM-FFN amplitudes do not exceed $20 \mu\text{atm}$ except for marginal seas where larger
discrepancies are calculated (6 of the 9 marginal MARCATS, Table S2). The monthly mean pCO_2 seasonal cycle simulated
by MOM6-COBALT is also well in phase (Pearson correlation coefficients > 0.5) with the one extracted from coastal-SOM-
330 FFN in 34 out of the 45 MARCATS (red colors in Fig. 5d and Table S2). The agreement is especially good in the best monitored
MARCATS regions (MARCATS where $> 50\%$ of the area is covered by Socatv6 observations, Table S1). For instance, in
regions with good data coverage such as along the East coast of the U.S (M10, Fig. 6a), the Norwegian Basin (M16, Fig. 6b),
the Californian Current (M2, Fig. 6c), the Leeuwin Current (M33), or the Brazilian Current (M6), the Pearson correlation
coefficient is higher than 0.9 (Table S2). In contrast, the seasonal pCO_2 cycle simulated by MOM6-COBALT substantially
335 diverges from that of the coastal-SOM-FFN in four poorly monitored marginal seas (M12, M21, M28, M29) and in a few of
the EBCs, Indian margins, subpolar margins (e.g., New Zealand, Fig. 6d) and tropical margins (Pearson correlation coefficient
 < 0.5 , Table S2 and blue colors in Fig. 5d).

3.1.3 Identifying coastal regions of 'high' model skill

Overall, the pCO_2 spatio-temporal analysis model-data evaluation shows that out of 45 MARCATS, 29 have an absolute bias
340 for their annual mean $< 20 \mu\text{atm}$ when MOM6-COBALT-coastal-SOM-FFN, MOM6-COBALT-Socatv6 and coastal-SOM-
FFN-Socatv6 are compared (Table S1). Together, these 29 MARCTAS represent 65 % of the global coastal ocean surface
area. For the 11 MARCATS that are best covered by observations (MARCATS where $> 50\%$ of the surface area is covered
by Socatv6 observations, Table S1), absolute biases for the annual mean are always $< 20 \mu\text{atm}$ for the three product
intercomparison, except in the Californian Current (M2), in the Baltic Sea (M18) and along the N-E Pacific (M1). The seasonal



345 MOM6-COBALT against coastal-SOM-FFN evaluation also reveal that 39 of the 45 MARCATS have $p\text{CO}_2$ seasonal amplitude biases $< 20 \mu\text{atm}$ and 34 MARCATS have a Pearson correlation coefficient > 0.5 (Table S2).

Based on this evaluation, we attribute for each MARCATS a level of confidence on the model skill ('high', 'medium' and 'low', Table 1 and Fig. 1a). Out of the 45 MARCATS, 25 are labeled as 'high' skill, that is to say, they fulfil the following
350 criteria regarding the annual mean and the seasonality (Table 1 and dotted MARCATS regions in Fig. 1a): a bias $< 20 \mu\text{atm}$ in the annual mean $p\text{CO}_2$ between MOM6-COBALT and coastal-SOM-FFN, a bias $< 20 \mu\text{atm}$ in the magnitude of the seasonal $p\text{CO}_2$ cycle and a seasonal phase characterized by a Pearson correlation coefficient > 0.5 . Note that these MARCATS but M43, M45, M1, M23 and M26 also present an annual mean $p\text{CO}_2$ bias $< 20 \mu\text{atm}$ in the MOM6-COBALT-Socativ6 and coastal-SOM-FFN-Socativ6 comparisons (Table S1). In addition, 7 'high skill' MARCATS also show a data density $> 50 \%$ (13
355 MARCATS if we lower the data coverage to $> 30 \%$, Fig. 1a). These 7 MARCATS are located in contrasted coastal environments, i.e. 3 EBCs (Iberian (M19) and Moroccan (M22) upwellings and the Leeuwin Current, M33), 1 WBC (East coast of the U.S, M10), 1 Polar (Norwegian Basin, M16), 1 subpolar (NE Atlantic, M17) and 1 marginal sea (Gulf of Mexico, M9). These 7 'high' skill MARCATS could also result from the very good correspondence on the data-model annual mean and seasonal patterns in environmental fields (Table S1 and Table S2 except M22, M33 and M9 for the nutrient phasing) and
360 are therefore excellent potential candidates for an analysis of the processes controlling the coastal $p\text{CO}_2$ dynamics. 6 additional MARCATS regions fulfil the criteria related to the seasonal $p\text{CO}_2$ evaluation while they fail to fulfil the annual mean $p\text{CO}_2$ bias threshold of $20 \mu\text{atm}$. These 'medium' skill regions (Table 1 and dashed regions in Fig. 1a) include 2 EBCs (Californian Current, M2 and SW Africa, M24), 1 marginal sea (Sea of Okhotsk, M41), 2 polar (Canadian Archipelago M13 and N Greenland, M14) and 1 subpolar (NW Pacific, M42) shelves. The majority of marginal seas are systematically associated with
365 large biases whether on the $p\text{CO}_2$ or on the main environmental variables. These regions fulfill only one or no criteria regarding the $p\text{CO}_2$ seasonality, and they are hence labeled as 'low' skill (Table 1, Fig. 1a). Other 'low' skill regions include 1 EBC (Peruvian upwelling Current, M4), 1 Indian (Bay of Bengal, M31), 2 tropical (Tropical E Pacific, M3 and SE Asia, M38), 2 subpolar (Sea of Labrador, M11 and New Zealand, M36) and 1 WBC (Brazilian Current, M6) margins.

3.1.4 Methodological limitations

370 While our results show a relatively good agreement between MOM6-COBALT and coastal-SOM-FFN regarding the spatial and temporal $p\text{CO}_2$ distribution over the global coastal ocean, the comparison remains challenging for several reasons.

First, while the climatology of Laruelle et al. (2017, coastal-SOM-FFN) is currently the best available product for a model-data comparison, it has its own limitations. For instance, in some regions, particularly coastal upwellings such as the Moroccan (M22) and Peruvian (M4) upwellings, the $p\text{CO}_2$ fields generated by the coastal-SOM-FFN do not reproduce well the high and
375 variable $p\text{CO}_2$ values measured in-situ (see e.g., Friederich et al., 2008 and McGregor et al., 2007). Such poor performance of the coastal-SOM-FFN algorithm in these types of systems were already identified by Laruelle et al. (2017). Indeed, upwelling



regions are still relatively poorly monitored and expand partly beyond the coastal domain used by Laruelle et al. (2017), leading to locally skewed calibration of the SOM-FFN. Deficiencies in the observation-based product can thus partly explain the large
380 model-data bias (106 μatm , largest of all MARCATS) calculated in the Peruvian upwelling region. Moreover, although the Surface Ocean CO_2 Atlas database (SOCAT) has expanded significantly over the past few years, some regions are still poorly monitored. In the coastal regions where no observational data exist (e.g., in the Black Sea, the Sea of Okhotsk, the Bay of Bengal, Fig. 4b) in the SOCAT database used here (SOCATv6, Bakker et al., 2016), it is difficult to evaluate the performance of the SOM-FFN and, thus, of an OGCM in reproducing the pCO_2 field. In addition, for certain regions subjected to complex
385 dynamic biogeochemical settings (e.g., upwelling, seasonal cover of sea-ice, influenced by rivers, marginal seas), the pCO_2 field reconstructed by the SOM-FFN suffers from poor performance, which can partly be explained by the lack of observational data. This lack of observations could partly explain why MOM6-COBALT-coastal-SOM-FFN pCO_2 biases exceed 20 μatm in these regions. This study highlights the regions (Fig.1a, e.g., Indian ocean margins, Peruvian upwelling, marginal seas) where new observational data are most urgently needed to improve our understanding of the CO_2 exchange between coastal
390 regions and the atmosphere at the regional and global scales. In addition, only one global continuous pCO_2 climatology derived by the SOM-FFN method currently exists for the coastal ocean. It would therefore be beneficial for the community to develop other observation-based climatologies relying on other interpolation techniques, as currently the case for the open ocean.

Second, the model-data comparison should also be analyzed in the light of the current limitations in the model itself. OGCMs
395 have been designed for global ocean applications and the coarse spatial resolution of these models, on the order of 0.5° in the present study, cannot resolve accurately mesoscale and sub-mesoscale processes as well as tidal mixing in shelf regions even with a model configuration including parameterizations for these processes. The coastal currents are also not always well resolved because of the coarse resolution of the shelf bathymetry. These small-scale hydrodynamic features are known to affect the spatio-temporal variability of pCO_2 and the air-sea CO_2 exchange (Bourgeois et al., 2016; Kelley et al., 1971; Lachkar et al., 2007; Laruelle et al., 2010). Therefore, although MOM6-COBALT runs at 0.5° , discrepancies between coastal-SOM-FFN
400 and MOM6-COBALT in narrow EBCs such as the Peruvian Upwelling Current (M4) and along South west Africa (M33) could also be explained by the limited spatial resolution of the model. Moreover, OGCMs such as MOM6-COBALT have a relatively simple representation of the biogeochemistry which does not fully captures some of the important processes of the carbon dynamics in coastal waters such as sea-ice temporal dynamics (Adcroft et al., 2019), neritic calcification (O'Mara and
405 Dunne, 2019), or terrestrial and marine organic matter decomposition and burial (Lacroix et al., 2021). Moreover, the largest biases observed in marginal seas can partly be explained by large fluvial inputs and oceanic water flows through fine scale topography (e.g. straits) that are poorly represented in global OGCMs.

Finally, the annual mean/seasonal pCO_2 biases between the coastal-SOM-FFN and MOM6-COBALT can also be traced back
410 to divergences in the environmental fields simulated by the model compared to observations (Table S1 and Table S2). For instance, in most marginal seas, the model poorly resolves the annual mean and seasonal cycle of SSS and nutrients compared



to the observations. These discrepancies impact the simulated $p\text{CO}_2$ via the controls of the SSS on the CO_2 solubility and of nutrients on the biological pump and CO_2 uptake. In the tropical W Atlantic (M7) which is under the influence of the Amazon River, the model simulates lower annual mean SSS (and therefore lower $p\text{CO}_2$) than the observations. In the tropical E Pacific (M3) and in South-East Asia (M38), the poor agreement between simulated and observed seasonal $p\text{CO}_2$ cycle could be explained by significant biases in the nutrient seasonal cycles (low Pearson correlation coefficient). Interestingly however, some regions reveal significant biases in the major environmental fields but not in the $p\text{CO}_2$ (e.g., Tropical W Atlantic, M7) while in other regions, the reverse is observed (e.g., M20, M27 and M36). Also, for some regions biases in environmental fields do not affect the $p\text{CO}_2$ as expected. For instance, along the East coast of the U.S (M10), MOM6-COBALT simulates larger SST compared to observations while the simulated $p\text{CO}_2$ is lower compared to coastal-SOM-FFN on an annual mean. This clearly shows that biases in environmental fields are not sufficient to explain fully the biases in $p\text{CO}_2$ diagnosed between MOM6-COBALT and coastal-SOM-FFN.

3.2 Processes governing the seasonal $p\text{CO}_2$ variability

Our second objective is to examine the drivers of the $p\text{CO}_2$ seasonality in three well sampled and contrasted coastal regions where the model skill is satisfactory: The East coast of North America (M10), the Norwegian Basin (M16) and the Californian Current (M2). The East coast of North America is a sink of atmospheric CO_2 that has been extensively studied over the past decade (e.g., Fennel et al., 2019; Laruelle et al., 2015; Shadwick et al., 2010, 2011; Signorini et al., 2013). The $p\text{CO}_2$ spatio-temporal dynamics in this MARCATS is particularly well captured by MOM6-COBALT ('high' skill, Fig. 1a), despite an annual mean SST bias of 1.3 °C on the data-model comparison in this region (Table S1). Because the SST amplitude and seasonal phasing are in agreement between the model and data (Table S2), the bias on the mean SST does not impact the seasonal $p\text{CO}_2$ cycle (Pearson correlation coefficient > 0.5 and bias $< 20 \mu\text{atm}$ on the seasonal $p\text{CO}_2$ amplitude, Table 1). We also selected the Californian Current because it is a source of CO_2 to the atmosphere, and similarly to the East coast of the U.S, it ranks among one of the best monitored coastal regions in the world (e.g., Evans et al., 2011; Fennel et al., 2019; Hales et al., 2012; Turi et al., 2014). In this region, the model is classified as 'medium' skill (Table 1 and Fig. 1a). Indeed, the simulated seasonal cycle of $p\text{CO}_2$ is in relatively good agreement with coastal-SOM-FFN (Figs. 5-6, and Table 1), despite biases in the annual mean $p\text{CO}_2$ compared to observations (Fig. 3f) and a phase shift in the seasonality of SSS and nutrients (Pearson correlation coefficient < 0.5). However, the Californian Current is also one of the few coastal regions where an analysis of the processes controlling the $p\text{CO}_2$ seasonality has already been performed using a regional biogeochemical model and sequential simulation removing processes one after the other (Turi et al., 2014), which can hence be compared to our analysis. Finally, the choice of the Norwegian Basin is motivated by the good performance ('high' skill) of the model and the intense atmospheric CO_2 sink that occurs in this contrasted region.



3.2.1 Seasonality along the East coast of North America

The seasonal evolution of pCO₂ averaged over the East coast of the U.S (M10) is represented in Fig. 7a. Ocean pCO₂ is minimum in winter (February/March ~ 331 μatm), it increases through spring and peaks in summer (August, ~ 400 μatm) before decreasing again in the fall. Figure 7b reveals the complex interplay of the four ocean internal processes (thermal, biology, ocean circulation, and fresh water flux) on the seasonal pCO₂ variability which can either act in synergy or oppose each other.

The thermal effect (*thermal*, red line on Fig. 7b) increases pCO₂ from early spring to summer by decreasing the solubility of CO₂. In contrast, the solubility of CO₂ increases in autumn and winter, inducing a decline in pCO₂. The largest changes in pCO₂ associated with the change in SST occur during spring (29 μatm month⁻¹ in June) and fall (-26 μatm month⁻¹ in November). This thermal effect was already identified by Signorini et al. (2013) in their observational study. These authors highlighted that lowest pCO₂ was generally reported in winter or at the beginning of spring and highest pCO₂ in summer or autumn, despite significant temporal and spatial heterogeneity between the different sub-regions of the East coast of the U.S (Scotian shelf, the Gulf of Maine, the Georges Bank/Nantucket shoals, the Middle Atlantic Bight, and the South Atlantic Bight). The effect of biology above the mixed layer depth (*bio*, green line) reduces pCO₂ throughout the year revealing that primary production exceeds organic matter degradation in the surface layer all year long. The largest pCO₂ decrease associated with biology is observed in early spring (values of -68 μatm month⁻¹ in April) which is well documented (e.g., Shadwick et al., 2010, 2011; Signorini et al., 2013). The transport of chemical species by ocean circulation (*circ*, blue line) increases pCO₂ and tends to oppose biology year-round except at the end of fall/beginning of winter. This pCO₂ increase induced by the circulation term is maximum in April (26 μatm month⁻¹). Throughout the year, the contribution of fresh water fluxes (*fw*, pink line) remains minor compared to the other terms (maximum absolute value of 9 μatm month⁻¹ in January). For each month/season, the air-sea CO₂ exchange term (*CO₂ flux*, black line) counteracts change in pCO₂ associated with ocean internal processes taking place in surface seawater (sum of *bio*, *circ*, *thermal* and *fw*). The *CO₂ flux* term increases pCO₂ at the sea-surface (acting as an atmospheric CO₂ sink) throughout the year except during summer (between July and September) where it decreases sea surface pCO₂ and releases CO₂ towards the atmosphere (acting as an atmospheric CO₂ source). This simulated atmospheric CO₂ uptake all year long except for the summer season is also in agreement with previous literature (Fennel et al., 2019; Laruelle et al., 2015; Signorini et al., 2013). The study of Laruelle et al. (2015) has nevertheless shown that in spring, the southern part of the Eastern North American coast is quasi neutral and that in fall, some regions such as the Gulf of Maine or the Georges Bank acts as a CO₂ source. The temporal change of pCO₂ (*pCO₂ change*, cyan line) is the result of the non-perfect balance between the internal processes and the air-sea CO₂ flux.

We evaluate the rate of change tied to each process during the marked peak-to-peak pCO₂ increase observed between winter and summer (from 331 μatm in February to 400 μatm in August, Fig. 7a). A positive rate of change (in μatm month⁻¹) indicates



475 that the process contributes to an increase in $p\text{CO}_2$ between winter and summer (February-August). This process-based analysis
reveals that the winter-to-summer $p\text{CO}_2$ increase in the East coast of the U.S (M10) mainly results from thermal (rate of change
= $+5 \mu\text{atm month}^{-1}$) and ocean circulation (rate of change = $+4 \mu\text{atm month}^{-1}$) influences combined with a large reduction of
the biological CO_2 uptake (rate change of $+7 \mu\text{atm month}^{-1}$, Fig. 7b). The importance of the thermal and circulation effects as
well as the presence of a strong biological drawdown are in line with results from past studies (e.g., Laruelle et al. (2015),
480 Shadwick et al. (2010, 2011) and Signorini et al. (2013)). Our results which identifies the reduction of biological carbon uptake
as a key control of $p\text{CO}_2$ seasonality agree with the studies of Shadwick et al. (2010, 2011), but slightly diverge compared to
those of Signorini et al. (2013) or Laruelle et al. (2015), which found that the thermal effect was the dominant driver. This
difference is largely explained by the different levels of details in the decomposition method. While most model studies,
including ours, use seasonal change in SST, SSS, DIC and ALK, observational approaches cannot isolate the compounding
485 changes tied to biological activity from those of ocean transport.

3.2.2 Seasonality in the Norwegian basin and in the Californian Current

The $p\text{CO}_2$ seasonal cycle in the Norwegian Basin (M16) and the Californian Current (M2) simulated by MOM6-COBALT are
represented in Fig. 7c and Fig. 7e, respectively. The Norwegian Basin shows a near-constant $p\text{CO}_2$ value ($\sim 330 \mu\text{atm}$)
throughout the year except in spring when it drops by $30 \mu\text{atm}$ (minimum $p\text{CO}_2$ value of $300 \mu\text{atm}$ in June). The phasing of
490 the seasonal $p\text{CO}_2$ cycle in the Californian Current is similar to that along the East coast of U.S, with a minimum $p\text{CO}_2$ value
of $366 \mu\text{atm}$ in March followed by an increase that reaches a maximum $p\text{CO}_2$ value of $433 \mu\text{atm}$ in August and then decreases
again at the beginning of the fall.

The decomposition of the seasonal cycle into different processes for both the Norwegian Basin and the Californian Current
495 (Fig. 7d and Fig. 7f) reveal patterns that are qualitatively similar to those already diagnosed for the East coast of the U.S (Fig.
7b). For both shelf regions, the biological and circulation effects respectively remain negative and positive throughout the year,
while the thermal effect increases $p\text{CO}_2$ in spring and summer but decreases $p\text{CO}_2$ in fall and winter. The fresh water term is
also minor compared to the other terms. Quantitatively, however, the amplitude of the different terms points to different first
order control in the $p\text{CO}_2$ seasonality for each region. The amplitudes are calculated here using the marked peak-to-peak
500 change in $p\text{CO}_2$ which occurs between February and June in the Norwegian basin and between March and August in the
Californian Current.

In the Norwegian basin, the strong winter to summer $p\text{CO}_2$ decreases ($43 \mu\text{atm}$, Fig. 7c) is mainly associated with the large
and rapid CO_2 uptake associated with the spring phytoplankton bloom (biological rate of change = $-45 \mu\text{atm month}^{-1}$ in average
505 between February and June and with a maximum $p\text{CO}_2$ uptake of $-175 \mu\text{atm month}^{-1}$ in June, Fig. 7d). This biological
drawdown is only partly compensated by the supply of high $p\text{CO}_2$ water masses by the ocean circulation (rate of change = $+24$
 $\mu\text{atm month}^{-1}$). This dynamics is consistent with the fact that the Norwegian Basin is one of the most productive region of the



world characterized by a well-documented, intense spring bloom (e.g., Findlay et al., 2008). In addition, the effect of thermal changes only plays a comparatively minor role here (rate of change = $+7 \mu\text{atm month}^{-1}$).

510

In contrast to the East coast of the U.S and the Norwegian Basin, the analysis performed in the Californian Current reveals that circulation is the main driver of the winter-to-summer pCO_2 increases ($68 \mu\text{atm}$, Fig 7e). The upwelling of high- pCO_2 waters increases surface pCO_2 year-round. Its influence is however weaker in winter than in summer, thereby explaining the pCO_2 increase observed between February and August (rate of change = $+12 \mu\text{atm month}^{-1}$, Fig. 7f). This large contribution from circulation is consistent with the simulations of Turi et al. (2014), which identified the ocean transport associated with upwelling in the Californian Current as the dominant process, and the higher intensity of the summer upwelling and its impact on pCO_2 was also reported in prior work (e.g., Evans et al., 2015; Fiechter et al., 2014; Turi et al., 2014). In this region, biology also opposes the effect of ocean circulation, with upwelled deep water bringing nutrients to the surface and stimulating phytoplankton productivity (e.g., Evans et al., 2015; Fiechter et al., 2014; Turi et al., 2014). However, it plays a minor role in the pCO_2 increase (rate of change $\sim 0 \mu\text{atm month}^{-1}$) as well as for the thermal effect (rate of change = $+4 \mu\text{atm month}^{-1}$).

520

4 Conclusions

In this study, an OGCM (MOM6-COBALT) which is primarily designed for the open ocean was used to examine sea surface pCO_2 seasonality in the coastal domain. We first evaluated the ability of the model to reproduce the spatial and temporal dynamics of key environmental variables, such as SST, SSS and sea surface nutrients against in-situ observations. The spatio-temporal variability of coastal pCO_2 was also evaluated using direct coastal pCO_2 observations from the SOCAT database (Socatv6, Bakker et al., 2016), and a global observational continuous monthly pCO_2 climatology available at high spatial resolution (coastal-SOM-FFN, Laruelle et al., 2017).

525

Our model-data comparison showed a relatively good agreement on the environmental variables spatio-temporal distribution except for some coastal regions mainly located in marginal seas. Our results also revealed a relatively good agreement between pCO_2 from MOM6-COBALT, coastal-SOM-FFN and Socatv6, both in time and space, and most of the discrepancies between the three products are found in regions with poor data coverage, such as in the Bay of Bengal, The Sea of Okhotsk or in the Hudson Bay (Fig. 1a). This study thus provides an objective framework to identify regions where new observational data collections are currently most needed to improve our global understanding of the CO_2 exchange between coastal regions and the atmosphere. From the model-data evaluation, we identified regions where the MOM6-COBALT model shows highest skill in reproducing the spatial and seasonal pCO_2 variability, and where the different processes governing the pCO_2 dynamics can be examined with reasonable confidence ('high' and 'medium' skill regions in Table 1 and Fig. 1a).

535



We also adapted a novel method to quantify the contributions of the different physical and biological processes governing the sea surface pCO₂ seasonality in the coastal domain. This method goes one step further than past coastal studies (e.g., Signorini et al., 2013; Turi et al., 2014) where the processes attribution was only based on the seasonal changes in DIC, ALK, SST and SSS or/and combined with a series of sequential simulations isolating one term after the other. In particular, our simulations are non-sequential and allow accounting for the co-variations between the different variables impacted by each process and how their simultaneous evolution modulates in quantitative terms the pCO₂ dynamics. Our approach, which is illustrated in three coastal regions (the East coast of the U.S, the California Current and the Norwegian Basin), allows to decipher the complex interplay between ocean transport of chemical species (DIC, ALK and SSS), biological drawdown, fresh water fluxes (dilution/concentration effects) and thermal changes (air-sea fluxes and transport of temperature) on the pCO₂ dynamics. Depending on the season and region, these terms can reinforce or oppose each other and act to strengthen or dampen the amplitude of pCO₂ seasonal variations that control the air-sea CO₂ exchange. Along the East Coast of the U.S and in the Californian Current, pCO₂ increases from winter-to-summer. In the former region, this increase is controlled by a subtle balance between biological drawdown, thermal changes and ocean circulation, while in the Californian Current, the circulation due to the upwelling (supplying pCO₂-rich waters to the surface) drives the increase in pCO₂. In contrast, in the Norwegian Basin, biological drawdown dominates the marked spring pCO₂ decrease observed in the region. These differences in the quantitative controls of pCO₂ dynamics from one region to another support our proposed analysis at the broad scale of the 45 MARCATS regions that together compose the global coastal ocean.

A handful of observational-based studies analyzed the seasonal variability of pCO₂ in the global coastal ocean (Cao et al., 2020; Chen and Hu, 2019; Laruelle et al., 2017). The mechanistic understanding of seasonal pCO₂ variations was, and remains limited by the amount of available observations. The modeling approach tailored for the coastal ocean presented in this manuscript complements observational studies and help improve our quantitative understanding of the underlying physical and biological drivers of the coastal pCO₂ dynamics. The comparison of the model performance to a state-of-the-art coastal pCO₂ database and continuous pCO₂ data product also lends confidence in our model results for a large fraction of the global coastal domain. The coastal ocean is under tremendous anthropogenic pressure (e.g. climate, land-use change and agriculture, pollution, urbanization; e.g., Mackenzie et al., 2005; Regnier et al., 2013; Seitzinger et al., 2005). Understanding the interplay between physics, biology and thermal processes and how they control coastal pCO₂ worldwide will be key to assess how their future changes impact air-sea CO₂ exchange in coastal environments.

Acknowledgements

L. Resplandy and E. Liao acknowledge the Cooperative Institute for Modeling the Earth System between NOAA GFDL and Princeton University, the Sloan Research foundation and the Princeton Catalysis Initiative. G. G. Laruelle is research associate of the F.R.S-FNRS at the Université Libre de Bruxelles. P. Regnier received financial support from BELSPO through the



project ReCAP, which is part of the Belgian research program FedTwin and from the European Union's Horizon 2020 research and innovation program VERIFY (grant agreement no. 776810) and ESM2025 projects

Data availability

- 575 The Surface Ocean CO₂ Atlas (SOCAT) is an international effort, endorsed by the International Ocean Carbon Coordination Project (IOCCP), the Surface Ocean Lower Atmosphere Study (SOLAS) and the Integrated Marine Biosphere Research (IMBeR) program, to deliver a uniformly quality-controlled surface ocean CO₂ database. The many researchers and funding agencies responsible for the collection of data and quality control are thanked for their contributions to SOCAT. Every previous version of the SOCAT database can also be accessed from the following page: <https://www.socat.info/index.php/previous-versions/>. The coastal-SOM-FFN pCO₂ datasets description and dataset can be downloaded from Laruelle et al. (2017). The SST and SSS used for the evaluation the model were extracted from the NOAA OI SST V2 (Reynolds et al., 2007) and the EN4 SSS (Good et al., 2013), respectively. Nutrients data were extracted from the World Ocean Atlas 2018 (Garcia et al., 2019). The delineation and description of the MARCATS segmentation can be found in Laruelle et al. (2013).
- 580

References

- 585 Adcroft, A., Anderson, W., Balaji, V., Blanton, C., Bushuk, M., Dufour, C. O., Dunne, J. P., Griffies, S. M., Hallberg, R., Harrison, M. J., Held, I. M., Jansen, M. F., John, J. G., Krasting, J. P., Langenhorst, A. R., Legg, S., Liang, Z., McHugh, C., Radhakrishnan, A., Reichl, B. G., Rosati, T., Samuels, B. L., Shao, A., Stouffer, R., Winton, M., Wittenberg, A. T., Xiang, B., Zadeh, N. and Zhang, R.: The GFDL Global Ocean and Sea Ice Model OM4.0: Model Description and Simulation Features, *J. Adv. Model. Earth Syst.*, doi:10.1029/2019MS001726, 2019.
- 590 Arruda, R., Calil, P. H. R., Bianchi, A. A., Doney, S. C., Gruber, N., Lima, I. and Turi, G.: Air-sea CO₂ fluxes and the controls on ocean surface pCO₂ seasonal variability in the coastal and open-ocean southwestern Atlantic Ocean: a modeling study, *Biogeosciences*, 12, 5793–5809, doi:10.5194/bg-12-5793-2015, 2015.
- Bakker, D. C. E., Pfeil, B., Landa, C. S., Metzl, N., O'Brien, K. M., Olsen, A., Smith, K., Cosca, C., Harasawa, S., Jones, S. D., Nakaoka, S. I., Nojiri, Y., Schuster, U., Steinhoff, T., Sweeney, C., Takahashi, T., Tilbrook, B., Wada, C., Wanninkhof, R., Alin, S. R., Balestrini, C. F., Barbero, L., Bates, N. R., Bianchi, A. A., Bonou, F. F., Boutin, J., Bozec, Y., Burger, E. F., Cai, W., Castle, R. D., Chen, L., Chierici, M., Currie, K., Evans, W., Featherstone, C., Feely, R. A., Fransson, A., Goyet, C., Greenwood, N., Gregor, L., Hankin, S., Hardman-Mountford, N. J., Harlay, J. J., Hauck, J., Hoppema, M., Humphreys, M. P., Hunt, C. W., Huss, B., Ibánhez, J. S. P., Johannessen, T., Keeling, R., Kitidis, V., Körtzinger, A., Kozyr, A., Krasakopoulou, E., Kuwata, A., Landschützer, P., Lauvset, S. K., Lefevre, N., Lo Monaco, C., Manke, A., Mathis, J. T., Merlivat, L., Millero, F. J., Monteiro, P. M. S., Munro, D. R., Murata, A., Newberger, T., Omar, A. M., Ono, T., Paterson, K., Pearce, D., Pierrot, D., Robbins, L. L., Saito, S., Salisbury, J., Schlitzer, R., Schneider, B., Schweitzer, R., Sieger, R., Skjelvan, I., Sullivan, K. F., Sutherland, S. C., Sutton, A. J., Tadokoro, K., Telszewski, M., Tuma, M., Van Heuven, S. M. A. C., Vandemark, D., Ward,
- 600



- B., Watson, A. J., Xu, S., Lefèvre, N., Monaco, C. Lo and Heuven, S. M. A. C. Van: A multi-decade record of high-quality fCO₂ data in version 3 of the Surface Ocean CO₂ Atlas (SOCAT), *Earth Syst. Sci. Data*, 8(2), 383–413, doi:10.5194/essd-8-383-2016, 2016.
- 605
- Borges, A. V., Delille, B. and Frankignoulle, M.: Budgeting sinks and sources of CO₂ in the coastal ocean: Diversity of ecosystem counts, *Geophys. Res. Lett.*, 32(14), 1–4, doi:10.1029/2005GL023053, 2005.
- Bourgeois, T., Orr, J. C., Resplandy, L., Terhaar, J., Ethé, C., Gehlen, M. and Bopp, L.: Coastal-ocean uptake of anthropogenic carbon, *Biogeosciences*, 13(14), 4167–4185, doi:https://doi.org/10.5194/bg-13-4167-2016, 2016.
- 610
- Cai, W.-J.: Estuarine and Coastal Ocean Carbon Paradox: CO₂ Sinks or Sites of Terrestrial Carbon Incineration?, *Ann. Rev. Mar. Sci.*, 3(1), 123–145, doi:10.1146/annurev-marine-120709-142723, 2011.
- Cao, Z., Yang, W., Zhao, Y., Guo, X., Yin, Z., Du, C., Zhao, H. and Dai, M.: Diagnosis of CO₂ dynamics and fluxes in global coastal oceans, *Natl. Sci. Rev.*, 7(4), 786–797, doi:10.1093/nsr/nwz105, 2020.
- Chen, C. T. A., Huang, T. H., Chen, Y. C., Bai, Y., He, X. and Kang, Y.: Air-sea exchanges of CO₂ in the world’s coastal seas, *Biogeosciences*, 10(10), 6509–6544, doi:10.5194/bg-10-6509-2013, 2013.
- 615
- Chen, S. and Hu, C.: Environmental controls of surface water pCO₂ in different coastal environments: Observations from marine buoys, *Cont. Shelf Res.*, 183, 73–86, doi:10.1016/j.csr.2019.06.007, 2019.
- Doney, S. C., Lima, I., Feely, R. A., Glover, D. M., Lindsay, K., Mahowald, N., Moore, J. K. and Wanninkhof, R.: Mechanisms governing interannual variability in upper-ocean inorganic carbon system and air–sea CO₂ fluxes: Physical climate and atmospheric dust, *Deep Sea Res. Part II Top. Stud. Oceanogr.*, 56(8–10), 640–655, doi:10.1016/j.dsr2.2008.12.006, 2009.
- 620
- Egleston, E. S., Sabine, C. L. and Morel, F. M. M.: Revelle revisited: Buffer factors that quantify the response of ocean chemistry to changes in DIC and alkalinity, *Global Biogeochem. Cycles*, 24(1), doi:10.1029/2008GB003407, 2010.
- Evans, W., Hales, B. and Strutton, P. G.: Seasonal cycle of surface ocean pCO₂ on the Oregon shelf, *J. Geophys. Res. Ocean.*, 116(5), doi:10.1029/2010JC006625, 2011.
- 625
- Evans, W., Hales, B., Strutton, P. G., Shearman, R. K. and Barth, J. A.: Failure to bloom: Intense upwelling results in negligible phytoplankton response and prolonged CO₂ outgassing over the Oregon shelf, *J. Geophys. Res. Ocean.*, 120(3), 1446–1461, doi:10.1002/2014JC010580, 2015.
- Fennel, K., Alin, S., Barbero, L., Evans, W., Bourgeois, T., Cooley, S., Dunne, J., Feely, R. A., Martin Hernandez-Ayon, J., Hu, X., Lohrenz, S., Muller-Karger, F., Najjar, R., Robbins, L., Shadwick, E., Siedlecki, S., Steiner, N., Sutton, A., Turk, D.,
- 630
- Vlahos, P. and Aleck Wang, Z.: Carbon cycling in the North American coastal ocean: A synthesis, *Biogeosciences*, 16(6), 1281–1304, doi:10.5194/bg-16-1281-2019, 2019.
- Fiechter, J., Curchitser, E. N., Edwards, C. A., Chai, F., Goebel, N. L. and Chavez, F. P.: Air-sea CO₂ fluxes in the California Current: Impacts of model resolution and coastal topography, *Global Biogeochem. Cycles*, 28(4), 371–385, doi:10.1002/2013GB004683, 2014.
- 635
- Findlay, H. S., Tyrrell, T., J. Bellerby, R. G., Merico, A. and Skjelvan, I.: Carbon and nutrient mixed layer dynamics in the Norwegian Sea, *Biogeosciences*, 5(5), 1395–1410, doi:10.5194/bg-5-1395-2008, 2008.



- Frankignoulle, M. and Borges, A. V.: European continental shelf as a significant sink for atmospheric carbon dioxide, *Global Biogeochem. Cycles*, 15(3), 569–576, doi:<https://doi.org/10.1029/2000GB001307>, 2001.
- 640 Friederich, G. E., Ledesma, J., Ulloa, O. and Chavez, F. P.: Air-sea carbon dioxide fluxes in the coastal southeastern tropical Pacific, *Prog. Oceanogr.*, 79(2–4), 156–166, doi:[10.1016/j.pocean.2008.10.001](https://doi.org/10.1016/j.pocean.2008.10.001), 2008.
- Friedlingstein, P., Jones, M. W., O’Sullivan, M., Andrew, R. M., Hauck, J., Peters, G. P., Peters, W., Pongratz, J., Sitch, S., Le Quéré, C., Bakker, D. C. E., Canadell, J. G., Ciais, P., Jackson, R. B., Anthoni, P., Barbero, L., Bastos, A., Bastrikov, V., Becker, M., Bopp, L., Buitenhuis, E., Chandra, N., Chevallier, F., Chini, L. P., Currie, K. I., Feely, R. A., Gehlen, M., Gilfillan, D., Gkritzalis, T., Goll, D. S., Gruber, N., Gutekunst, S., Harris, I., Haverd, V., Houghton, R. A., Hurtt, G., Ilyina, T., Jain, A. K., Joetzjer, E., Kaplan, J. O., Kato, E., Goldewijk, K. K., Korsbakken, J. I., Landschützer, P., Lauvset, S. K., Lefèvre, N., Lenton, A., Lienert, S., Lombardozi, D., Marland, G., McGuire, P. C., Melton, J. R., Metzl, N., Munro, D. R., Nabel, J. E. M. S., Nakaoka, S. I., Neill, C., Omar, A. M., Ono, T., Peregón, A., Pierrot, D., Poulter, B., Rehder, G., Resplandy, L., Robertson, E., Rödenbeck, C., Séférian, R., Schwinger, J., Smith, N., Tans, P. P., Tian, H., Tilbrook, B., Tubiello, F. N., Van Der Werf, G. R., Wiltshire, A. J. and Zaehle, S.: Global carbon budget 2019, *Earth Syst. Sci. Data*, 11(4), 1783–1838, doi:[10.5194/essd-11-1783-2019](https://doi.org/10.5194/essd-11-1783-2019), 2019.
- 650 Garcia, H. E., Locarnini, R. A., Boyer, T. P., Antonov, J. I., Baranova, O. K., Zweng, M. M., Reagan, J. R. and Johnson, D. R.: World Ocean Atlas 2013. Volume 3. dissolved oxygen, apparent oxygen utilization, and oxygen saturation, NOAA Atlas NESDIS 75, 3, 27, 2013a.
- Garcia, H. E., Locarnini, R. A., Boyer, T. P., Antonov, J. I., Baranova, O. K., Zweng, M. M., Reagan, J. R., Johnson, D. R. and Mishonov, A. V.: World ocean atlas 2013. Volume 4. Dissolved inorganic nutrients (phosphate, nitrate, silicate), NOAA Atlas NESDIS 76, 4, 25, doi:[10.7289/V5J67DWD](https://doi.org/10.7289/V5J67DWD), 2013b.
- Garcia, H. E., Weathers, K. W., Paver, C. R., Smolyar, I., Boyer, T. P., Locarnini, R. A., Zweng, M. M. and A.V. Mishonov, O.K. Baranova, D. Seidov, and J. R. R. (: NOAA Atlas World Ocean Atlas 2018. Vol. 4: Dissolved Inorganic Nutrients (phosphate, nitrate and nitrate+nitrite, silicate)., 2019.
- 660 Good, S. A., Martin, M. J. and Rayner, N. A.: EN4: Quality controlled ocean temperature and salinity profiles and monthly objective analyses with uncertainty estimates, *J. Geophys. Res. Ocean.*, 118(12), 6704–6716, doi:[10.1002/2013JC009067](https://doi.org/10.1002/2013JC009067), 2013.
- Gruber, N., Gloor, M., Mikaloff Fletcher, S. E., Doney, S. C., Dutkiewicz, S., Follows, M. J., Gerber, M., Jacobson, A. R., Joos, F., Lindsay, K., Menemenlis, D., Mouchet, A., Müller, S. A., Sarmiento, J. L. and Takahashi, T.: Oceanic sources, sinks, and transport of atmospheric CO₂, *Global Biogeochem. Cycles*, 23(1), 1–21, doi:[10.1029/2008GB003349](https://doi.org/10.1029/2008GB003349), 2009.
- 665 Gruber, N., Clement, D., Carter, B. R., Feely, R. A., Van Heuven, S., Hoppema, M., Ishii, M., Key, R. M., Kozyr, A., Lauvset, S. K., Lo Monaco, C., Mathis, J. T., Murata, A., Olsen, A., Perez, F. F., Sabine, C. L., Tanhua, T. and Wanninkhof, R.: The oceanic sink for anthropogenic CO₂ from 1994 to 2007, *Science* (80-.), 363(6432), 1193–1199, doi:[10.1126/science.aau5153](https://doi.org/10.1126/science.aau5153), 2019.
- 670 Hales, B., Strutton, P. G., Saraceno, M., Letelier, R., Takahashi, T., Feely, R., Sabine, C. and Chavez, F.: Satellite-based



- prediction of pCO₂ in coastal waters of the eastern North Pacific, *Prog. Oceanogr.*, 103, 1–15, doi:10.1016/j.pocean.2012.03.001, 2012.
- Joos, F. and Spahni, R.: Rates of change in natural and anthropogenic radiative forcing over the past 20,000 years, *Proc. Natl. Acad. Sci. U. S. A.*, 105(5), 1425–1430, doi:10.1073/pnas.0707386105, 2008.
- 675 Keeling, R. F. and Manning, A. C.: Studies of Recent Changes in Atmospheric O₂ Content, in *Treatise on Geochemistry* (Second Edition), pp. 385–404., 2014.
- Kelley, J. J., Longerich, L. L. and Hood, D. W.: Effect of upwelling, mixing, and high primary productivity on CO₂ concentrations in surface waters of the Bering Sea, *J. Geophys. Res.*, 76(36), 8687–8693, doi:10.1029/jc076i036p08687, 1971.
- Khatiwala, S., Tanhua, T., Mikaloff Fletcher, S., Gerber, M., Doney, S. C., Graven, H. D., Gruber, N., McKinley, G. A.,
680 Murata, A., Ríos, A. F. and Sabine, C. L.: Global ocean storage of anthropogenic carbon, *Biogeosciences*, 10(4), 2169–2191, doi:10.5194/bg-10-2169-2013, 2013.
- Lachkar, Z., Orr, J. C., Dutay, J. C. and Delectase, P.: Effects of mesoscale eddies on global ocean distributions of CFC-11, CO₂, and Δ14C, *Ocean Sci.*, 3(4), 461–482, doi:10.5194/os-3-461-2007, 2007.
- Lacroix, F., Ilyina, T., Laruelle, G. G. and Regnier, P.: Reconstructing the Preindustrial Coastal Carbon Cycle Through a
685 Global Ocean Circulation Model: Was the Global Continental Shelf Already Both Autotrophic and a CO₂ Sink?, *Global Biogeochem. Cycles*, 35(2), e2020GB006603, doi:10.1029/2020GB006603, 2021.
- Landschützer, P., Gruber, N., Bakker, D. C. E. and Schuster, U.: Recent variability of the global ocean carbon sink, *Global Biogeochem. Cycles*, 28(9), 927–949, doi:10.1002/2014GB004853, 2014.
- Landschützer, P., Gruber, N., Bakker, D. C. E., Stemmler, I. and Six, K. D.: Strengthening seasonal marine CO₂ variations
690 due to increasing atmospheric CO₂, *Nat. Clim. Chang.*, doi:10.1038/s41558-017-0057-x, 2018.
- Laruelle, G. G., Dürr, H. H., Slomp, C. P. and Borges, A. V.: Evaluation of sinks and sources of CO₂ in the global coastal ocean using a spatially-explicit typology of estuaries and continental shelves, *Geophys. Res. Lett.*, 37(15), 1–6, doi:10.1029/2010GL043691, 2010.
- Laruelle, G. G., Dürr, H. H., Lauerwald, R., Hartmann, J., Slomp, C. P., Goossens, N. and Regnier, P.: Global multi-scale
695 segmentation of continental and coastal waters from the watersheds to the continental margins, *Hydrol. Earth Syst. Sci.*, 17(5), 2029–2051, doi:10.5194/hess-17-2029-2013, 2013.
- Laruelle, G. G., Lauerwald, R., Pfeil, B. and Regnier, P.: Regionalized global budget of the CO₂ exchange at the air-water interface in continental shelf seas, *Global Biogeochem. Cycles*, 28, 1199–1214, doi:10.1002/2014GB004832, 2014.
- Laruelle, G. G., Lauerwald, R., Rotschi, J., Raymond, P. A., Hartmann, J. and Regnier, P.: Seasonal response of air-water CO₂
700 exchange along the land-ocean aquatic continuum of the northeast North American coast, *Biogeosciences*, 12(5), 1447–1458, doi:10.5194/bg-12-1447-2015, 2015.
- Laruelle, G. G., Landschützer, P., Gruber, N., Tison, J. L., Delille, B. and Regnier, P.: Global high-resolution monthly pCO₂ climatology for the coastal ocean derived from neural network interpolation, *Biogeosciences*, 14(19), 4545–4561, doi:10.5194/bg-14-4545-2017, 2017.



- 705 Laruelle, G. G., Cai, W.-J., Hu, X., Gruber, N., Mackenzie, F. T. and Regnier, P.: Continental shelves as a variable but increasing global sink for atmospheric carbon dioxide, *Nat. Commun.*, 9(1), 454, doi:10.1038/s41467-017-02738-z, 2018.
- Lewis, E. R. and Wallace, D. W. R.: Program developed for CO₂ system calculations, *Environmental System Science Data Infrastructure for a Virtual Ecosystem.*, 1998.
- Liao, E., Resplandy, L., Liu, J. and Bowman, K. W.: Amplification of the Ocean Carbon Sink During El Niños: Role of Poleward Ekman Transport and Influence on Atmospheric CO₂, *Global Biogeochem. Cycles*, 34(9),
710 doi:10.1029/2020GB006574, 2020.
- Liu, K. K., Atkinson, L., Quiñones, R. and Talaue-McManus, L.: *Carbon and Nutrient Fluxes in Continental Margins*, Springer Science & Business Media., 2010.
- Locarnini, R. A., Mishonov, A. V., Antonov, J. I., Boyer, T. P., Garcia, H. E., Baranova, O. K., Zweng, M. M., Paver, C. R.,
715 Reagan, J. R., Johnson, D. R., Hamilton, M. and Seidov, D.: World ocean atlas 2013. Volume 1, Temperature, NOAA Atlas NESDIS 73, 1, 40, doi:10.7289/V55X26VD, 2013.
- Lovenduski, N. S., Gruber, N., Doney, S. C. and Lima, I. D.: Enhanced CO₂ outgassing in the Southern Ocean from a positive phase of the Southern Annular Mode, *Global Biogeochem. Cycles*, 21(2), n/a-n/a, doi:10.1029/2006GB002900, 2007.
- Mackenzie, F. T., Andersson, A. J., Lerman, A. and Ver, L. M.: Boundary exchanges in the global coastal margin: implications
720 for the organic and inorganic carbon cycles, *sea*, 13, 193–225, 2005.
- Manning, A. C. and Keeling, R. F.: Global oceanic and land biotic carbon sinks from the scripps atmospheric oxygen flask sampling network, *Tellus, Ser. B Chem. Phys. Meteorol.*, 58(2), 95–116, doi:10.1111/j.1600-0889.2006.00175.x, 2006.
- McGregor, H. V., Dima, M., Fischer, H. W. and Mulitza, S.: Rapid 20th-century increase in coastal upwelling off northwest Africa, *Science (80-)*, 315(5812), 637–639, doi:10.1126/science.1134839, 2007.
- 725 Millero, F. J.: Carbonate constants for estuarine waters, *Mar. Freshw. Res.*, 61(2), 139–142, doi:10.1071/MF09254, 2010.
- Nakaoka, S. I., Aoki, S., Nakazawa, T., Hashida, G., Morimoto, S., Yamanouchi, T. and Yoshikawa-Inoue, H.: Temporal and spatial variations of oceanic pCO₂ and air-sea CO₂ flux in the Greenland Sea and the Barents Sea, *Tellus, Ser. B Chem. Phys. Meteorol.*, 58(2), 148–161, doi:10.1111/j.1600-0889.2006.00178.x, 2006.
- O’Mara, N. A. and Dunne, J. P.: Hot Spots of Carbon and Alkalinity Cycling in the Coastal Oceans, *Sci. Rep.*, 9(1),
730 doi:10.1038/s41598-019-41064-w, 2019.
- Olsen, A., Key, R. M., Van Heuven, S., Lauvset, S. K., Velo, A., Lin, X., Schirnack, C., Kozyr, A., Tanhua, T., Hoppema, M., Jutterström, S., Steinfeldt, R., Jeansson, E., Ishii, M., Pérez, F. F. and Suzuki, T.: The global ocean data analysis project version 2 (GLODAPv2) - An internally consistent data product for the world ocean, *Earth Syst. Sci. Data*, 8(2), 297–323, doi:10.5194/essd-8-297-2016, 2016.
- 735 Regnier, P., Friedlingstein, P., Ciais, P., Mackenzie, F. T., Gruber, N., Janssens, I. A., Laruelle, G. G., Lauerwald, R., Luyssaert, S., Andersson, A. J., Arndt, S., Arnosti, C., Borges, A. V., Dale, A. W., Gallego-Sala, A., Goddérís, Y., Goossens, N., Hartmann, J., Heinze, C., Ilyina, T., Joos, F., LaRowe, D. E., Leifeld, J., Meysman, F. J. R., Munhoven, G., Raymond, P. A., Spahni, R., Suntharalingam, P. and Thullner, M.: Anthropogenic perturbation of the carbon fluxes from land to ocean, *Nat.*

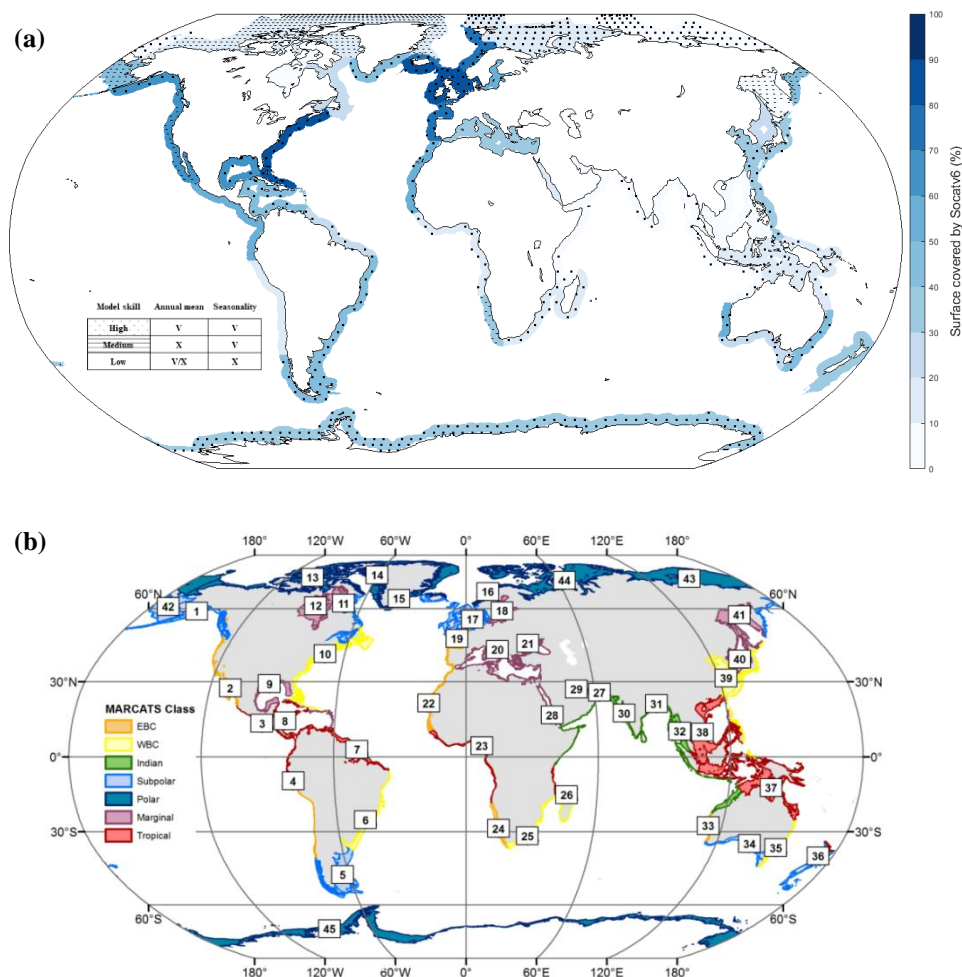


- Geosci., 6(8), 597–607, doi:10.1038/ngeo1830, 2013.
- 740 Reynolds, R. W., Smith, T. M., Liu, C., Chelton, D. B., Casey, K. S. and Schlax, M. G.: Daily high-resolution-blended analyses for sea surface temperature, *J. Clim.*, 20(22), 5473–5496, doi:10.1175/2007JCLI1824.1, 2007.
- Rödenbeck, C., Bakker, D. C. E., Metzl, N., Olsen, A., Sabine, C., Cassar, N., Reum, F., Keeling, R. F. and Heimann, M.: Interannual sea–air CO₂ flux variability from an observation-driven ocean mixed-layer scheme, *Biogeosciences*, 11(17), 4599–4613, doi:10.5194/bg-11-4599-2014, 2014.
- 745 Rödenbeck, C., Bakker, D. C. E., Gruber, N., Iida, Y., Jacobson, A. R., Jones, S., Landschützer, P., Metzl, N., Nakaoka, S., Olsen, A., Park, G. H., Peylin, P., Rodgers, K., Sasse, T. P., Schuster, U., Shutler, J. D., Valsala, V., Wanninkhof, R. and Zeng, J.: Data-based estimates of the ocean carbon sink variability - First results of the Surface Ocean pCO₂ Mapping intercomparison (SOCOM), *Biogeosciences*, 12(23), 7251–7278, doi:10.5194/bg-12-7251-2015, 2015.
- Roobaert, A., Laruelle, G. G., Landschützer, P., Gruber, N., Chou, L. and Regnier, P.: The Spatiotemporal Dynamics of the
750 Sources and Sinks of CO₂ in the Global Coastal Ocean, *Global Biogeochem. Cycles*, doi:10.1029/2019GB006239, 2019.
- Sarmiento, J. L. and Gruber, N.: *Ocean Biogeochemical Dynamics*, Princeton University Press., 2006.
- Seitzinger, S. P., Harrison, J. A., Dumont, E., Beusen, A. H. W. and Bouwman, A. F.: Sources and delivery of carbon, nitrogen, and phosphorus to the coastal zone: An overview of Global Nutrient Export from Watersheds (NEWS) models and their application, *Global Biogeochem. Cycles*, 19(4), doi:10.1029/2005GB002606, 2005.
- 755 Shadwick, E. H., Thomas, H., Comeau, A., Craig, S. E., Hunt, C. W. and Salisbury, J. E.: Air-sea CO₂ fluxes on the Scotian Shelf: Seasonal to multi-annual variability, *Biogeosciences*, 7(11), 3851–3867, doi:10.5194/bg-7-3851-2010, 2010.
- Shadwick, E. H., Thomas, H., Azetsu-Scott, K., Greenan, B. J. W., Head, E. and Horne, E.: Seasonal variability of dissolved inorganic carbon and surface water pCO₂ in the Scotian Shelf region of the Northwestern Atlantic, *Mar. Chem.*, 124(1–4), 23–37, doi:10.1016/j.marchem.2010.11.004, 2011.
- 760 Signorini, S. R., Mannino, A., Najjar, R. G., Friedrichs, M. A. M., Cai, W. J., Salisbury, J., Wang, Z. A., Thomas, H. and Shadwick, E.: Surface ocean pCO₂ seasonality and sea-air CO₂ flux estimates for the North American east coast, *J. Geophys. Res. Ocean.*, 118(10), 5439–5460, doi:10.1002/jgrc.20369, 2013.
- Stock, C. A., Dunne, J. P. and John, J. G.: Global-scale carbon and energy flows through the marine planktonic food web: An analysis with a coupled physical-biological model, *Prog. Oceanogr.*, 120, 1–28, doi:10.1016/j.pocean.2013.07.001, 2014.
- 765 Stock, C. A., Dunne, J. P., Fan, S., Ginoux, P., John, J., Krasting, J. P., Laufkötter, C., Paulot, F. and Zadeh, N.: Ocean Biogeochemistry in GFDL’s Earth System Model 4.1 and Its Response to Increasing Atmospheric CO₂, *J. Adv. Model. Earth Syst.*, 12(10), doi:10.1029/2019MS002043, 2020.
- Takahashi, T., Olafsson, J., Goddard, J. G., Chipman, D. W. and Sutherland, S. C.: Seasonal variation of CO₂ and nutrients in the high-latitude surface oceans: A comparative study, *Global Biogeochem. Cycles*, 7(4), 843–878, doi:10.1029/93GB02263,
770 1993.
- Takahashi, T., Sutherland, S. C., Sweeney, C., Poisson, A., Metzl, N., Tilbrook, B., Bates, N., Wanninkhof, R., Feely, R. a, Sabine, C., Olafsson, J. and Nojiri, Y.: Global sea – air CO₂ flux based on climatological surface ocean pCO₂, and seasonal

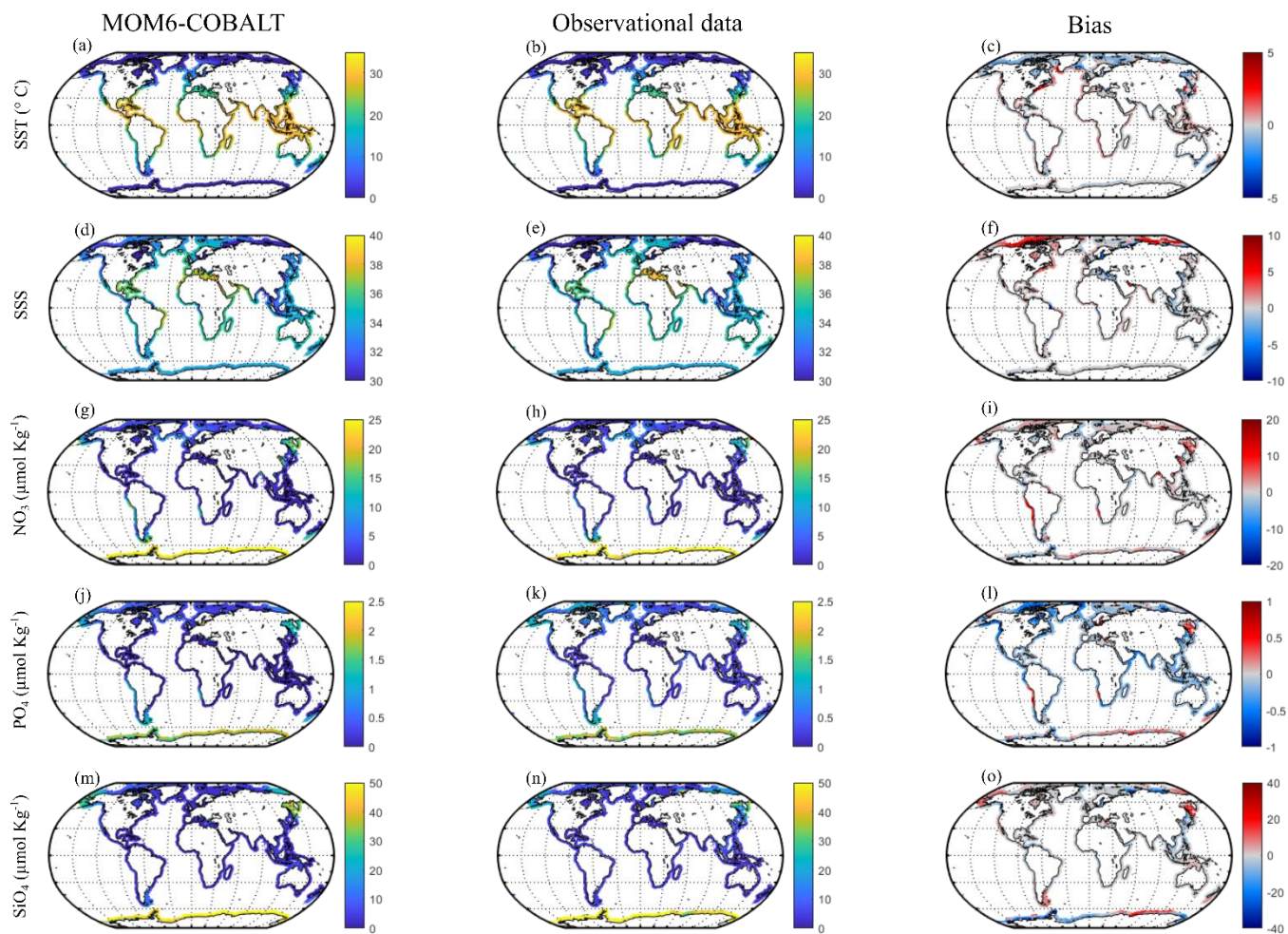


- biological and temperature effects, *Deep Sea Res. Part II Top. Stud. Oceanogr.*, 49(9–10), 1601–1622, doi:10.1016/S0967-0645(02)00003-6, 2002.
- 775 Takahashi, T., Sutherland, S. C. and Kozyr, A.: Global ocean surface water partial pressure of CO₂ database: Measurements performed during 1957–2011 (Version 2011), Carbon Dioxide Inf. Anal. Center, Oak Ridge Natl. Lab. US Dep. Energy, Oak Ridge, Tennessee, 2012.
- Tsujino, H., Urakawa, S., Nakano, H., Small, R. J., Kim, W. M., Yeager, S. G., Danabasoglu, G., Suzuki, T., Bamber, J. L., Bentsen, M., Böning, C. W., Bozec, A., Chassignet, E. P., Curchitser, E., Boeira Dias, F., Durack, P. J., Griffies, S. M., Harada,
- 780 Y., Ilicak, M., Josey, S. A., Kobayashi, C., Kobayashi, S., Komuro, Y., Large, W. G., Le Sommer, J., Marsland, S. J., Masina, S., Scheinert, M., Tomita, H., Valdivieso, M. and Yamazaki, D.: JRA-55 based surface dataset for driving ocean–sea-ice models (JRA55-do), *Ocean Model.*, 130, 79–139, doi:10.1016/j.ocemod.2018.07.002, 2018.
- Turi, G., Lachkar, Z. and Gruber, N.: Spatiotemporal variability and drivers of pCO₂ and air-sea CO₂ fluxes in the California Current System: An eddy-resolving modeling study, *Biogeosciences*, 11(3), 671–690, doi:10.5194/bg-11-671-2014, 2014.
- 785 Wolf-Gladrow, D. A., Zeebe, R. E., Klaas, C., Körtzinger, A. and Dickson, A. G.: Total alkalinity: The explicit conservative expression and its application to biogeochemical processes, *Mar. Chem.*, 106(1-2 SPEC. ISS.), 287–300, doi:10.1016/j.marchem.2007.01.006, 2007.
- Yasunaka, S., Murata, A., Watanabe, E., Chierici, M., Fransson, A., van Heuven, S., Hoppema, M., Ishii, M., Johannessen, T., Kosugi, N., Lauvset, S. K., Mathis, J. T., Nishino, S., Omar, A. M., Olsen, A., Sasano, D., Takahashi, T. and Wanninkhof, R.:
- 790 Mapping of the air-sea CO₂ flux in the Arctic Ocean and its adjacent seas: Basin-wide distribution and seasonal to interannual variability, *Polar Sci.*, 10(3), 323–334, doi:10.1016/j.polar.2016.03.006, 2016.
- Zweng, M. M., Reagan, J. R., Antonov, J. I., Locarnini, R. A., Mishonov, A. V., Boyer, T. P., Garcia, H. E., Baranova, O. K., Johnson, D. R., Seidov, Dan, 1948- and Biddle, M. M.: World ocean atlas 2013. Volume 2, Salinity, NOAA Atlas NESDIS 74, 2, 39, doi:10.7289/V5251G4D, 2013.

795

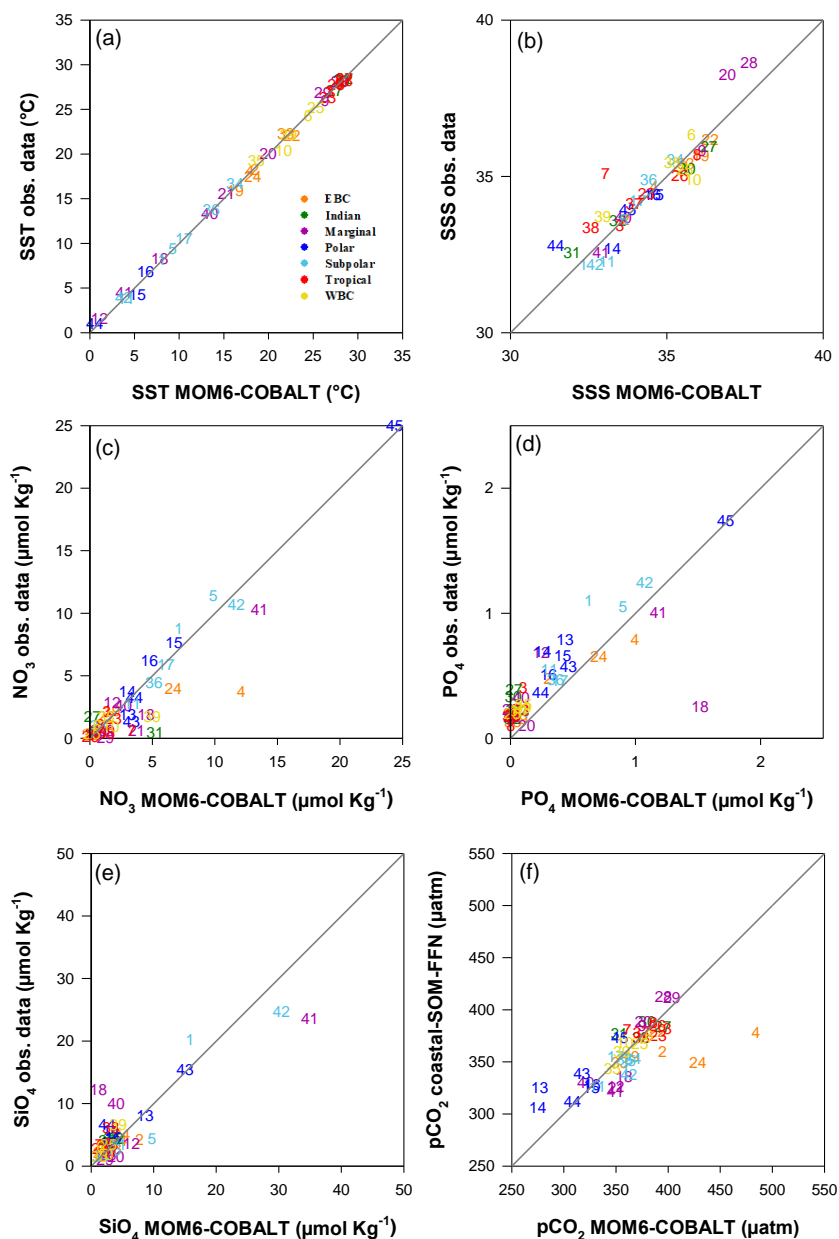


800 **Figure 1:** (a) Data coverage (color) and model skill (symbols) in coastal MARCATS (Margins and CATCHment Segmentation)
 regions. The blue intensity indicates the fraction of the MARCATS' surface area covered by Socatv6 observations (from light to
 805 dark blue). Dots indicate where the model fulfils three evaluation criteria ('high' skill regions) on the spatio-temporal pCO₂
 distribution (i.e., annual mean mismatch < 20 μatm between MOM6-COBALT and coastal-SOM-FFN, Pearson correlation
 coefficient > 0.5 and seasonal amplitude mismatch < 20 μatm). Dashes indicate where the model only fulfils two criteria (seasonal
 810 amplitude and phase, 'medium' skill). Other's regions ('low' skill with no symbol) do not fulfil the two criteria associated with
 seasonality. Details on model skill are in Table 1. (b) Discretization of the coastal seas into 45 MARCATS (Laruelle et al., 2013)
 grouped into seven classes: Eastern (MARCATS 2, 4, 19, 22, 24, and 33) and Western (MARCATS 6, 10, 25, 35, and 39) boundary
 currents (EBC and WBC, respectively), polar (MARCATS 13, 14, 15, 16, 43, 44, and 45) and subpolar margins (MARCATS 1, 5,
 11, 17, 34, 36, and 42), tropical margins (MARCATS 3, 7, 8, 23, 26, 37, and 38), Indian margins (MARCATS 27, 30, 31, and 32), and
 marginal seas (MARCATS 9, 12, 18, 20, 21, 28, 29, 40, and 41).



815 **Figure 2:** Observed (center) and modeled (left) spatial distributions of the annual mean state of SST ($^{\circ}\text{C}$), SSS (no unit), nitrate (NO_3 , $\mu\text{mol kg}^{-1}$), phosphate (PO_4 , $\mu\text{mol kg}^{-1}$) and silicate (SiO_4 , $\mu\text{mol kg}^{-1}$), and model annual mean bias (right). Observational SST and SSS fields are from the NOAA OI SST V2 (Reynolds et al., 2007) and the EN4 SSS (Good et al., 2013). Observational nutrients are from the World Ocean Atlas version 2018 (Garcia et al., 2019). The bias is the difference between MOM6-COBALT and observed values (red indicate regions where the simulated variables by MOM6-COBALT exceed observed values).

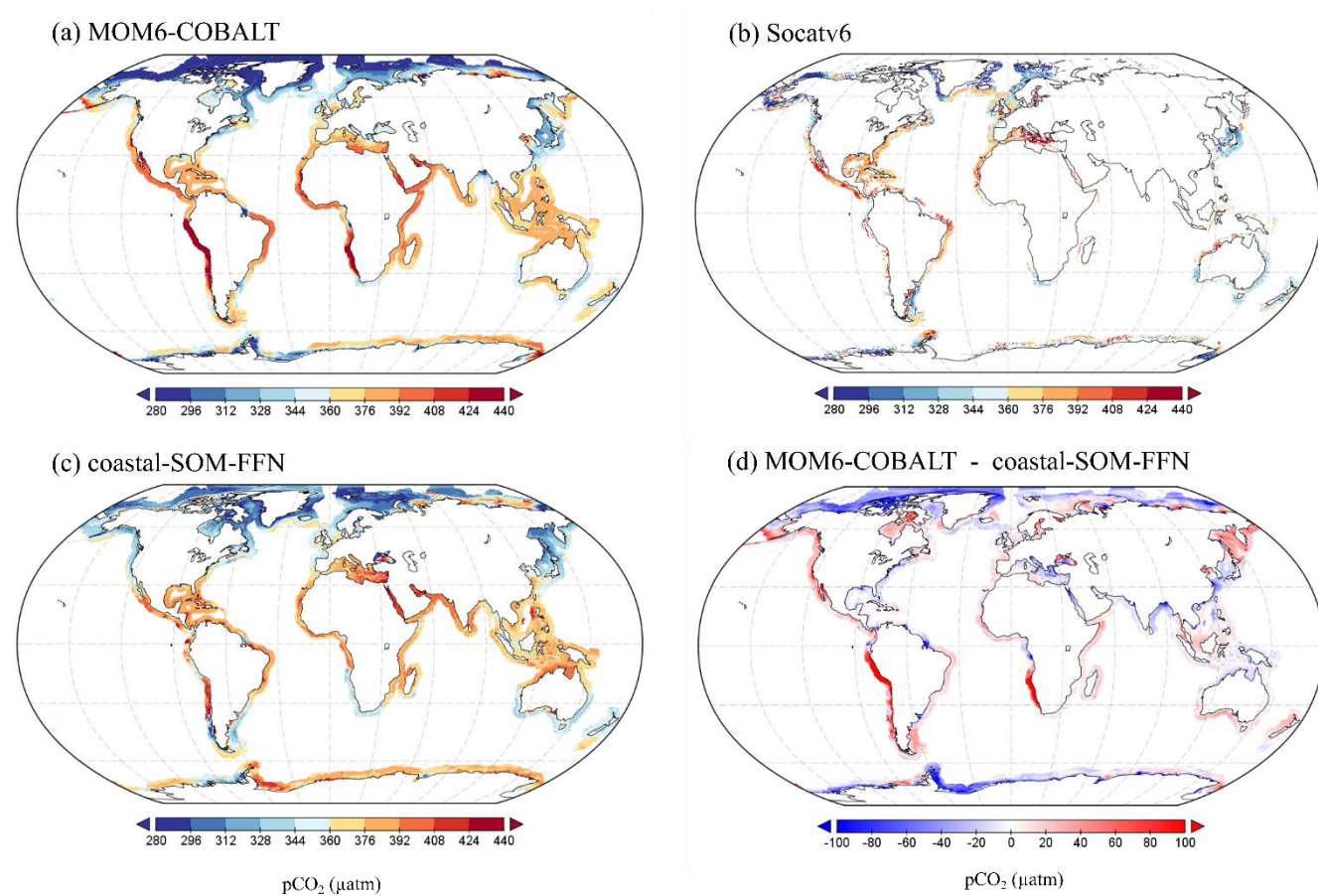
820



825 **Figure 3: Comparison between observed and simulated annual mean fields in the 45 MARCATS regions: (a) SST (°C), (b) SSS (no unit), (c) NO₃ (µmol kg⁻¹), (d) PO₄ (µmol kg⁻¹), (e) SiO₄ (µmol kg⁻¹) and (f) pCO₂ (µatm). Observational datasets: SST and SSS are from the NOAA OI SST V2 (Reynolds et al., 2007) and the EN4 SSS (Good et al., 2013), nutrients are from the World Ocean Atlas 2018 (Garcia et al., 2019), pCO₂ is from the coastal-SOM-FFN product (Laruelle et al., 2017). Colors correspond to the seven major MARCATS classes (see Fig. 1b). In panels (d) and (e), the Black Sea (M21) is not represented and has a xy coordinated of (0.2; 3.5 µmol kg⁻¹) in panel (d) and (10.3; 83.1 µmol kg⁻¹) in panel (e). The Antarctic shelf (M45) is also not represented in panel (e) (55.0; 49.1 µmol kg⁻¹).**



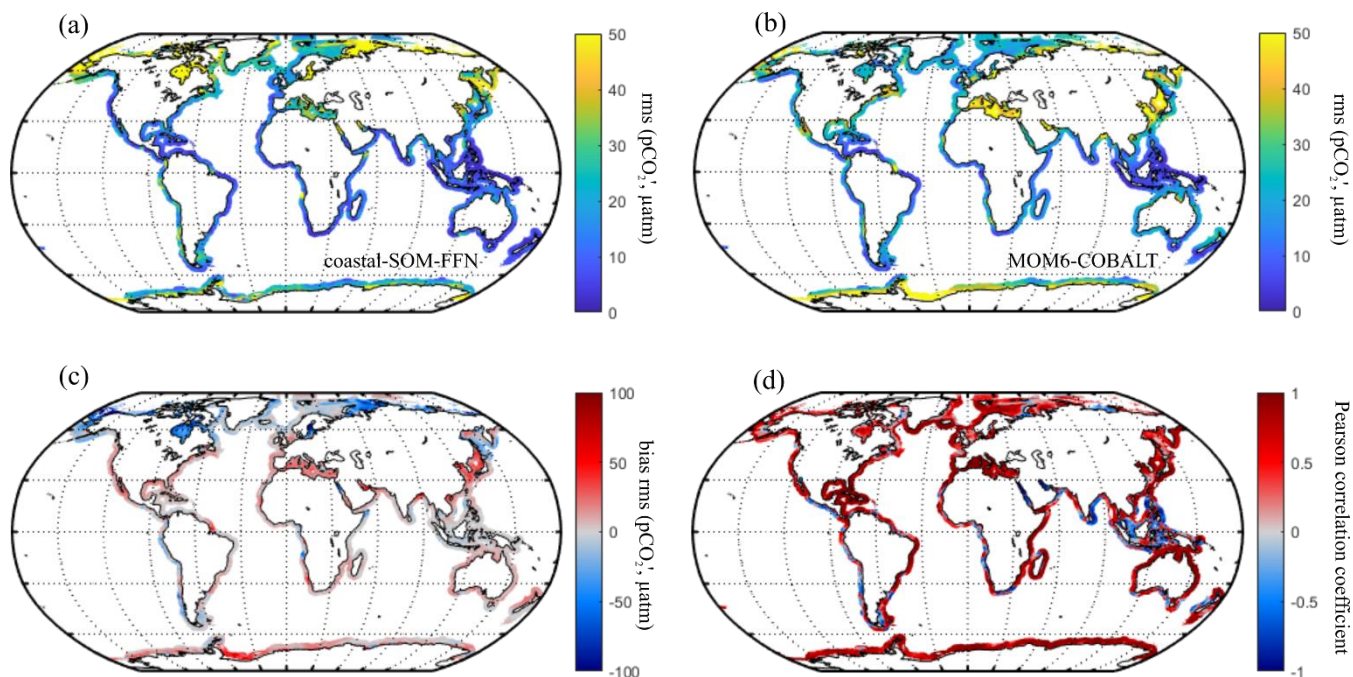
830



835

Figure 4: Spatial distributions of the annual mean $p\text{CO}_2$ (μatm) generated by (a) MOM6-COBALT, (b) extracted from the Socatv6 database and (c) from the coastal-SOM-FFN product (Laruelle et al., 2017). (d) Model bias as difference between panels (a) and (c) in μatm (red colors correspond to regions in which the $p\text{CO}_2$ simulated by MOM6-COBALT is higher than coastal-SOM-FFN).

840



845 **Figure 5: Seasonal variability in ocean pCO₂ (µatm). Seasonal amplitude (a) in the coastal-SOM-FFN product, (b) simulated by MOM6-COBALT model, (c) bias between model and coastal-SOM-FFN seasonal amplitude (red indicate simulated amplitude exceeds coastal-SOM-FFN). The seasonal amplitude is expressed as the root-mean-square of the monthly climatology pCO₂ anomalies (RMS_{pCO_2} , µatm). (d) Pearson correlation coefficient of the regression between the seasonal pCO₂ cycles calculated by MOM6-COBALT and coastal-SOM-FFN. A value of 1 indicates that both signals are perfectly in phase with one another while a value of -1 represents a complete phase shift.**



850

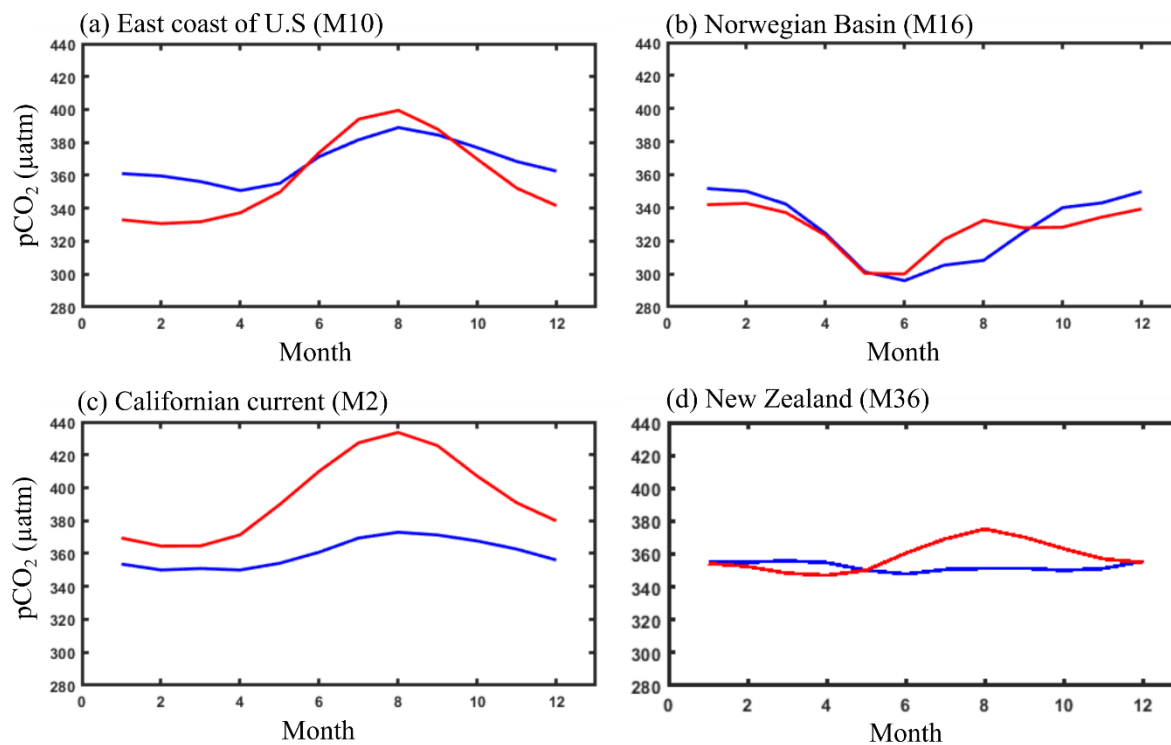


Figure 6: Seasonal pCO₂ cycle (µatm) derived from coastal-SOM-FFN (in blue) and simulated by MOM6-COBALT (in red) for (a) the East coast of the U.S (M10), (b) the Norwegian Basin (M16), (c) the West coast of North America (M2) and for (d) New Zealand (M36). Month 1 corresponds to January.

855

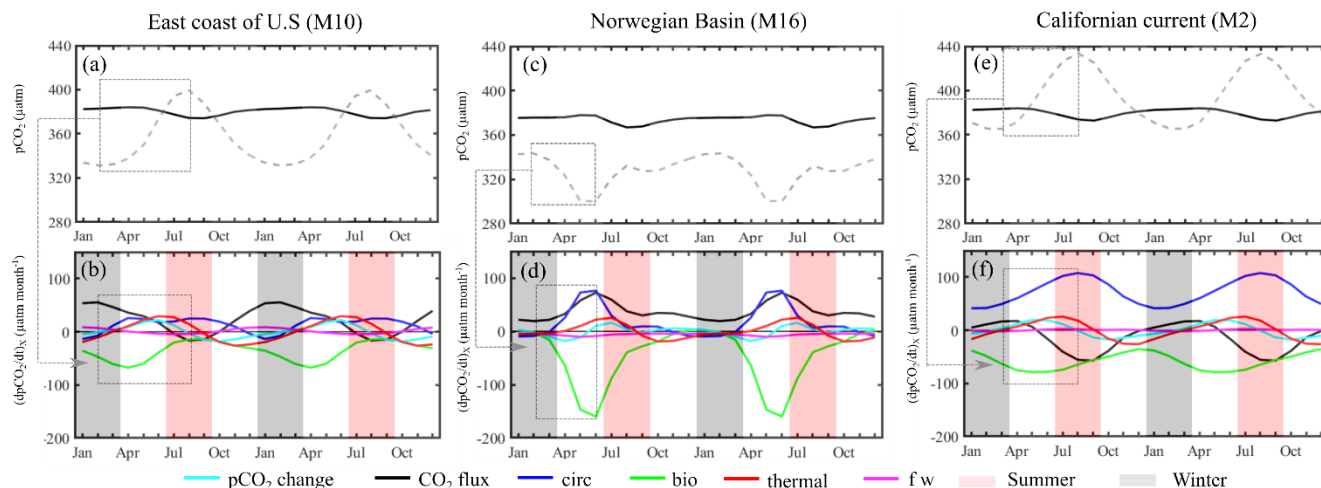


Figure 7: Processes controlling ocean pCO₂ seasonal cycle. Mean seasonal sea surface pCO₂ (dashed line) and atmospheric pCO₂ (black line) in μatm simulated by MOM6-COBALT and detrended over (a) the East coast of the US (M10) and (c) the Norwegian sea (M16) and (e) the Californian current (M2). Spatially averaged contributions (in μatm month⁻¹) from biological activity (*bio*, green), temperature changes (*thermal*, red), transport of chemical species (*circ*, blue), freshwater flux (*fw*, pink) and the CO₂ air-sea flux (*CO₂ flux*, black) controlling the pCO₂ temporal change (*pCO₂ change*, cyan) for the three regions (b, d and f). A positive value corresponds to an increase in sea surface pCO₂. Winter corresponds to the months of January, February and March, and Summer to the months of July, August and September.

860

865



870

Table 1: Model skill level. For each MARCAT, the model skill (‘high’, ‘medium’ and ‘low’) is attributed from the pCO₂ spatio-temporal analysis. Regions where the model fulfils criteria on the annual mean and seasonality are labelled as ‘high’ skill regions (i.e., annual mean mismatch < 20 µatm between MOM6-COBALT and coastal-SOM-FFN, Pearson correlation coefficient > 0.5 and seasonal amplitude mismatch < 20 µatm, dots in Fig. 1a). High* skill region can present a bias > 20 µatm on the comparison with Socatv6 (see Table S1). ‘Medium’ skill regions represent MARCATS where the model only fulfils seasonal criteria (seasonal amplitude and phase, dashed in Fig. 1a). Other’s regions (‘low’ skill) do not fulfil the two criteria associated to the seasonality (no symbol in Fig. 1a). Regions with ‘high’ model skill are considered as the most robust for an in-depth analysis of the processes driving the coastal pCO₂ dynamics and are highlighted in bold on the Table.

MARCATS number (Mx)	MARCATS name	MARCATS category	Annual mean pCO ₂ (µatm)		Seasonal pCO ₂			Model skill
			Coastal-SOM-FFN	Model bias	Amplitude (µatm)		Phasing (Pearson coefficient)	
					Coastal-SOM-FFN RMS	Model bias		
2	Californian Current	EBC	360.0	34.5	8.3	16.2	1.0	Medium
4	Peruvian upwelling Current	EBC	377.6	106.4	4.1	6.6	-0.4	Low
19	Iberian upwelling	EBC	354.8	9.3	7.5	15.6	0.8	High
22	Moroccan upwelling	EBC	379.4	10.2	7.4	8.7	0.9	High
24	SW Africa	EBC	349.1	79.3	7.2	4.2	0.9	Medium
33	Leeuwin Current	EBC	349.4	4.2	5.6	12.7	0.9	High
27	W Arabian Sea	Indian margins	383.5	11.6	8.7	3.6	0.3	Low
30	E Arabian Sea	Indian margins	388.4	-8.3	4.8	6.2	0.7	High
31	Bay of Bengal	Indian margins	377.3	-24.1	7.4	13.5	-0.2	Low
32	Tropical E Indian	Indian margins	373.3	0.3	2.3	5.4	0.9	High
9	Gulf of Mexico	Marginal sea	384.3	-9.1	13.9	12.9	1.0	High
12	Hudson Bay	Marginal sea	326.4	5.7	65.3	-46.4	0.4	Low
18	Baltic Sea	Marginal sea	336.2	21.4	79.4	-44.4	0.9	Low
20	Mediterranean Sea	Marginal sea	388.1	-11.9	25.1	20.6	1.0	Low
21	Black Sea	Marginal sea	325.0	25.2	141.9	-116.9	-0.5	Low
28	Red Sea	Marginal sea	412.2	-16.5	25.0	-0.4	-0.9	Low
29	Persian Gulf	Marginal sea	411.2	-7.6	31.3	30.7	-0.9	Low
40	Sea of Japan	Marginal sea	330.3	-9.3	21.1	28.0	0.9	Low
41	Sea of Okhotsk	Marginal sea	321.2	29.2	28.6	-6.5	0.7	Medium
13	Canadian Archipelago	Polar	325.4	-53.1	43.4	-18.0	0.9	Medium



14	N Greenland	Polar	306.0	-24.3	21.7	-9.0	0.8	Medium
15	S Greenland	Polar	325.2	1.3	24.5	-8.5	1.0	High
16	Norwegian Basin	Polar	328.1	-0.7	19.9	-6.1	0.9	High
43	Siberian Shelves	Polar	338.2	-19.7	57.4	-15.7	0.9	High*
44	Barents and Kara seas	Polar	311.6	-3.3	24.9	-7.4	0.7	High
45	Antarctic Shelves	Polar	373.7	-17.6	22.6	13.3	1.0	High*
1	N-E Pacific	Subpolar	342.5	16.8	15.8	-4.5	0.8	High*
5	Southern America	Subpolar	351.1	14.0	12.1	-6.4	0.8	High
11	Sea of Labrador	Subpolar	326.3	5.5	17.0	0.8	0.2	Low
17	NE Atlantic	Subpolar	354.4	-4.5	14.9	-8.2	0.6	High
34	S Australia	Subpolar	352.7	13.5	3.7	12.8	0.9	High
36	New Zealand	Subpolar	352.4	6.1	2.6	6.2	-0.5	Low
42	NW Pacific	Subpolar	337.7	25.2	36.5	-19.2	1.0	Medium
3	Tropical E Pacific	Tropical	382.2	17.2	6.9	3.1	0.3	Low
7	Tropical W Atlantic	Tropical	380.3	-19.8	2.8	9.6	1.0	High
8	Caribbean Sea	Tropical	387.6	-1.7	6.6	2.2	1.0	High
23	Tropical E Atlantic	Tropical	374.6	15.9	2.9	1.5	0.6	High*
26	Tropical W Indian	Tropical	384.8	4.8	7.1	5.6	0.9	High*
37	N Australia	Tropical	378.5	-4.0	4.3	5.2	1.0	High
38	SE Asia	Tropical	373.5	0.6	2.6	8.9	0.2	Low
6	Brazilian Current	WBC	374.8	7.0	6.7	7.5	0.9	High
10	East coast of US	WBC	368.1	-9.6	12.0	12.4	0.9	High
25	Agulhas Current	WBC	367.1	5.7	7.1	8.1	1.0	High
35	E Australian Current	WBC	343.9	2.9	3.3	7.4	1.0	High
39	China Sea and Kuroshio	WBC	359.6	-4.1	10.3	13.2	0.9	High